Landslides (2016) 13:653–670
DOI 10.1007/s10346-015-0592-3
Received: 22 September 2014
Accepted: 4 June 2015
Published online: 5 July 2015

A. Vallet · J. B. Charlier · O. Fabbri · C. Bertrand · N. Carry · J. Mudry

Functioning and precipitation-displacement modelling of rainfall-induced deep-seated landslides subject to creep deformation

Abstract We propose an approach to study the hydro-mechanical behaviour and evolution of rainfall-induced deep-seated landslides subjected to creep deformation by combining signal processing and modelling. The method is applied to the Séchilienne landslide in the French Alps, where precipitation and displacement have been monitored for 20 years. Wavelet analysis is first applied on precipitation and recharge as inputs and then on displacement time-series decomposed into trend and detrended signals as outputs. Results show that the detrended displacement is better linked to the recharge signal than to the total precipitation signal. The infra-annual detrended displacement is generated by high precipitation events, whereas annual and multi-annual variations are rather linked to recharge variations and thus to groundwater processes. This leads to conceptualise the system into a two-layer aquifer constituted of a perched aquifer (reactive aquifer responsible of high-frequency displacements) and a deep aquifer (inertial aquifer responsible of low-frequency displacements). In a second step, a new lumped model (GLIDE) coupling groundwater and a creep deformation model is applied to simulate displacement on three extensometer stations. The application of the GLIDE model gives good performance, validating most of the preliminary functioning hypotheses. Our results show that groundwater fluctuations can explain the displacement periodic variations as well as the long-term creep exponential trend. In the case of deep-seated landslides, this displacement trend is interpreted as the consequence of the weakening of the rock mechanical properties due to repeated actions of the groundwater pressure.

Keywords Creep deformation · Displacement pattern · Wavelet analysis · Lumped model · Deep-seated landslide

Introduction

Groundwater recharge is a key triggering factor for landslide destabilisation by decreasing the resistance of materials due to pore water pressure variations (Van Asch et al. 1999; Iverson 2000; Cappa et al. 2004; Corominas et al. 2005; Bogaard et al. 2007). Hydro-mechanical processes which lead to slope failure of deep-seated landslides are complex and are influenced by the evolution of the landslide deformation through time (Iverson 2000; Brunsden 2001; Rutqvist and Stephansson 2003; Binet et al. 2007; Prokešová et al. 2013). This is especially true in the case of deep-seated landslides subject to long-term creep deformation (Saito 1969; Chigira 1992; Brückl 2001; Bonzanigo et al. 2007; de Blasio 2011; Federico et al. 2012). Long-term creep mechanism is characterised by time-dependent deformation of rock masses under stress (Federico et al. 2012). The deformation reduces the whole landslide strength through the weakening of the slope material (Chigira 1992). Besides, in the case of landslides with irregular displacement patterns, a strength increase by consolidation may occur during periods at rest (Nieuwenhuis 1991; Angeli et al. 2004). For landslides experiencing such deformation processes, the modelling of landslide deformation requires the use of "dynamic" models instead of classical "static" models by introducing time-dependent components (Brunsden 2001; Corominas et al. 2005; Du et al. 2013).

Few studies focused on landslide creep deformation since such approaches require to perform long-term analyses and thus require multi-annual records of time-series (Corominas et al. 2005; Guglielmi et al. 2005; Zangerl et al. 2010; Klimeš et al. 2011; Brückl et al. 2013; Crosta et al. 2015). There is indeed a need to improve the understanding of landslide creep deformation for which only sparse data limited to rainfall and displacement are generally available. For that, investigating rainfall-displacement relationships can help to characterise hydro-mechanical processes (Matsuura et al. 2008). The non-linear features of these relationships justify the use of adapted signal processing methods such as the wavelet analysis which gives, unlike the classical Fourier analysis used to study stationary systems, a time-frequency localisation of the processes. Wavelet analysis is a powerful technique commonly used in geosciences (Kumar and Foufoula-Georgiou 1997; Torrence and Compo 1998; Labat et al. 2000; Jevrejeva et al. 2003; Grinsted et al. 2004; Maraun and Kurths 2004). By decomposing a time-series into time-scale space, this method can identify power variations of the signal. It is ideal for analysing non-stationary signals and for identifying short-scale to large-scale periodic phenomena. Wavelet analysis has recently been used with success in hydrogeology to study rainfall-groundwater and rainfall-runoff relationships of karst springs (Labat et al. 2000; Massei et al. 2006; Charlier et al. 2015). To our knowledge, no application on rainfall-displacement data has been carried out in order to characterise the hydro-mechanical response of landslides to rainfall.

Two types of numerical models for displacement simulation or prediction are generally used: (1) black-box models which quantify the rainfall-displacement relationships and (2) physically based models which integrate hydrogeological and mechanical landslide properties. Black-box (or input-output) models are generally lumped, considering the landslide area as one entity, whereas physical-based models can be spatially distributed. Various black-box models can be used: the transfer function model (Belle et al. 2014; Abellán et al. 2014), the neural network model (Liu et al. 2005; Du et al. 2013) and the inverse function model (Li et al. 1996). Such modelling methods are simple and parsimonious. However, few of these models take into account time-dependent factors which exert significant controls on landslide creep deformation (Li et al. 1996; Du et al. 2013). Although black-box models show accurate performance and simplicity to be integrated in a warning system, they do not emphasise physical process and therefore can be limited in the understanding of the landslide-control

mechanisms. Conversely, physically based models (Cappa et al. 2004, 2014; Corominas et al. 2005; Guglielmi et al. 2005; Malet et al. 2005; Tacher et al. 2005; van Asch et al. 2007) provide a good understanding of the failure mechanisms and integrate time-dependent factors. These models require numerous in situ geophysical, geotechnical or hydrodynamic measurements. The acquisition of these data is complex (even impossible) because of the continuously moving landslide mass. Moreover, these data are often poorly representative of the spatial variations of the landslide properties, especially in the case of scattered measurements. Consequently, the necessary parameters are often seldom monitored. Lastly, these models are far from routine and their operational applicability in a warning system is limited (Corominas et al. 2005). Hybrid models combining black-box groundwater models with physically based mechanical models (Angeli et al. 1998; Bernardie et al. 2014) allow an intermediary level of investigation and are more appropriated for landslide prediction. Nevertheless, these models still require in situ measurements.

Reservoir lumped models can be used to decipher the complexity of the hydrogeological systems by considering each reservoir (e.g. soil, perched aquifer, deep aquifer) as a storage element of the hydrosystem (Angeli et al. 1998; Charlier et al. 2012). This kind of model may be an acceptable compromise between empirical black-box models and distributed models which are physically consistent but remain difficult to implement. A reliable model needs precisely characterised hydrogeological and hydro-mechanical systems in order to relate model parameters to physically meaningful concepts. Using time-series decomposition, Du et al. (2013) showed that both long-term trend and residual short-term periodic components can be modelled separately since their hydro-mechanical mechanisms have various origins. This suggests that preliminary time-series decomposition is a promising approach for new reservoir modelling methods accounting for the main hydrogeological processes and their role on landslide displacement.

This paper aims at characterising hydro-mechanical processes by investigating rainfall-displacement relationships using wavelet analysis and also at developing a reservoir model to simulate displacement of rainfall-induced landslides subject to creep deformation. The approach combines two steps. First, a wavelet analysis carried out on decomposed time-series is performed in order to separate the effects on the landslide displacement velocities of precipitation or recharge from the effects of long-term creep deformation. Considering the hydrogeological context, this analysis allows to build a landslide conceptual model. Second, a new time-dependent lumped reservoir hydro-mechanical model is developed to simulate the short-term periodic displacement variations as well as the long-term creep trend from the precipitation data series. The proposed method is applied to the Séchilienne landslide in the French Alps where precipitations and displacement have been monitored for 20 years.

Signal processing method

Statistical time-series decomposition

The decomposition of time-series is a statistical method that separates a time-series into several distinct components. Three components are of interest: a deterministic non-seasonal long-term trend component T_t, a deterministic seasonal component S_t with a known periodicity and a stochastic irregular component I_t (or "noise") that describes erratic fluctuations. The seasonal component refers here to a statistical term which includes all periodic variations of a time-series. The irregular component represents the residuals of the signal after the trend and the seasonal component are removed from the time-series (Madsen 2007; Cowpertwait and Metcalfe 2009; Aragon 2011). The two S_t and I_t components contribute to the detrended component D_t.

Two statistical decomposition methods are generally used for representing a time-series y_t as a function of its trend, seasonal and irregular components: the additive decomposition method and the multiplicative decomposition method. The additive decomposition method (Eq. (1)) is generally more appropriate when the magnitudes of the seasonal component and the irregular component remain constant over time, i.e. independent of the trend time-series (Madsen 2007).

$$y_t = T_t + S_t + I_t \text{ with } D_t = S_t + I_t \quad (1)$$

On the contrary, the multiplicative decomposition method (Eq. (2)) is generally more appropriate when the magnitudes of the seasonal component and the irregular component change proportionally with the trend of the series (Madsen 2007).

$$y_t = T_t S_t I_t \text{ with } D_t = S_t I_t \quad (2)$$

S_t and I_t fluctuate around 0 or around 1 for the additive and multiplicative decomposition, respectively. In some cases and notably when the measurement frequency is within the same range as the high-frequency fluctuations of the time-series, we can assume that it is negligible, leading to decompose y_t into a trend component T_t and a detrended component D_t.

Wavelet analysis

The wavelet analysis method used in this paper is briefly presented on the basis of definitions put forward by several authors in geosciences (Kumar and Foufoula-Georgiou 1997; Torrence and Compo 1998; Labat et al. 2000; Jevrejeva et al. 2003; Grinsted et al. 2004; Maraun and Kurths 2004). The equations for wavelet analysis are given in the Appendix. The wavelet analysis method allows to decompose a time-series over a time-frequency space, thus providing a visualisation of the amplitude of any "periodic" signal within the series and how this amplitude varies with time. It is suitable for the analysis of non-stationary processes that contain multi-scale features, for detection of singularities, or for transient phenomena (Kumar and Foufoula-Georgiou 1997). Thus, the wavelet analysis gives a time-frequency representation of the processes and of their relationships.

The continuous wavelet transform (CWT) can be seen as a succession of bandpass filters of uniform shapes and varying locations and widths (Torrence and Compo 1998). CWT is thus characterised at the time-frequency space (hereafter referred to as time-scale space) by a window decreasing in width when focusing on local-scale structures (high frequencies) and increasing in width when focusing on large-scale structures (low frequencies). As CWTs are applied to time-series of finite lengths, edge effects may appear on the wavelet power spectrum (or scalogram), leading to the definition of a cone of influence (COI) in the region where such effects are significant (Torrence and Compo 1998). The

COI is computed at the 95 % confidence level and is marked by attenuated colour intensities on the scalogram. Many geophysical time-series have distinctive red noise characteristics (Grinsted et al. 2004). The 5 % significance level of the wavelet power against red noise is shown as a thick contour on the scalogram. Only the identified patches within the thick contours and outside of the COI region can be reliably interpreted.

The covariance between two time-series x and y is estimated using a cross wavelet transform (XWT, also called a cross-scalogram) which is the convolution product of the scalogram of both x and y signals. The XWT reveals patch areas with a high common power value. XWT is jointly used with wavelet coherence (WTC) which is a measure of the covariance intensity of the two series in the time-frequency space. A causality relationship is interpreted for patches having synchronic common high powers on XWT and WTC. The choice of the appropriate wavelet analysis depends on the nature of the signal and on the type of information to be extracted from the time-series (De Moortel et al. 2004). In this study, the Morlet wavelet is used because it is fairly well localised in the time-frequency space (Torrence and Compo 1998). The Paul and Mexican hat (DOG) wavelet basis functions were also tested, but gave poorer results than the Morlet wavelet.

A multi-resolution analysis (MRA) is used to decompose a signal into a progression of successive approximations and details in increasing order of resolution. In this study, a multi-resolution using "Daubechies-20" wavelet is carried out to filter the times series, removing outliers by the isolation of the noisy component in the high frequencies.

Continuous wavelet analyses (CWT, XWT and WTC) were carried out using a free Matlab software package (Mathworks, Natick, MA) provided by Grinsted et al. (2004) at http://noc.ac.uk/using-science/crosswavelet-wavelet-coherence. The package includes a code originally written by C. Torrence and G. Compo, available at http://paos.colorado.edu/research/wavelets/, and by E. Breitenberger of the University of Alaska, adapted from the freeware SSA-MTM Toolkit: http://www.atmos.ucla.edu/tcd/ssa/. MRA was carried out using a free Matlab software package provided by the WaveLab Development Team and available at http://statweb.stanford.edu/~wavelab/.

Numerical modelling of precipitation-displacement velocity

Model structure and governing equations

The groundwater landslide displacement creep (GLIDE) model aims at simulating the landslide displacement, using a reservoir hydro-mechanical model coupling a groundwater model and a landslide creep model. The structure and the parameters of the model are given in Fig. 1 and Table 1.

The GLIDE model is a lumped model, which can be applied in a semi-distributed approach. In this type of model, a complex and spatially distributed system is first simplified by one or several discrete entities which can be or not inter-dependent. The behaviour of each entity is then described by one or several lumped parameters. Lastly, the combination of the behaviour of each entity accounts for the behaviour of the entire system. Intrinsically, a lumped model does not allow to relate the lumped parameters to specific or detailed physical processes internal to an entity but allow to describe the global behaviour. The GLIDE model accounts for direct or indirect hydro-mechanical couplings (Rutqvist and Stephansson 2003). Concerning indirect hydro-mechanical couplings, the GLIDE model just takes into account the possible variations of the rock mechanical properties but not those of the hydraulic properties.

The landslide displacement is decomposed into two components according to the multiplicative method detailed in the "Statistical time-series decomposition" section. The detrended component is assumed to be linked to the groundwater trigger effect, whereas the trend is assumed to result from a long-term rock weakening of the landslide strength. The detrended displacement and the displacement trend are modelled separately using a groundwater model and a landslide creep model, respectively. After that, a re-composition of the global signal is done to simulate the displacement time-series.

Groundwater model: detrended displacement

The hydrogeology of deep-seated landslides generally shows a high hydraulic conductivity gradient between the near-surface unstable zone and the deep fractured rocks. This organisation leads to a two-layer aquifer system constituted by a perched aquifer, hosted by the near-surface disturbed rock mass, disconnected from a deep aquifer (Van Asch et al. 1999; Guglielmi et al. 2002; Binet et al. 2007; Pisani

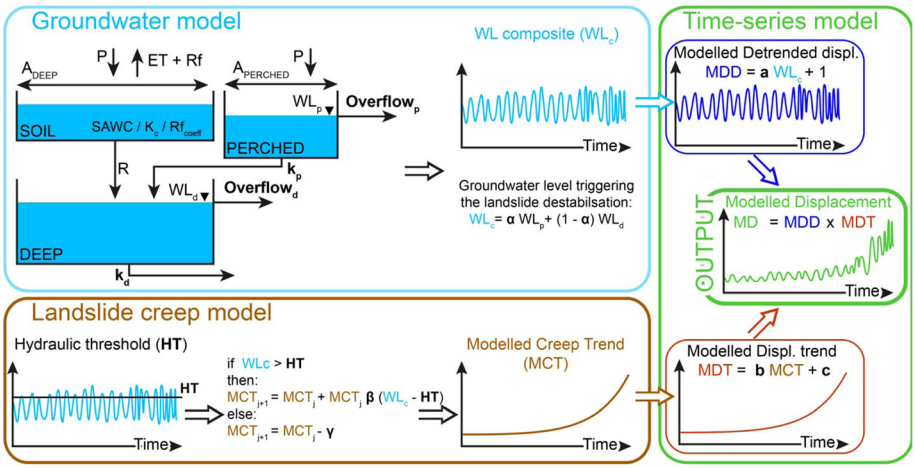

Fig. 1 Structure of the GLIDE model. *Parameters in bold* correspond to the model parameters that are to be estimated

Table 1 Parameters of the numerical model: description and calibration results for scenario 1 (S1) and scenario 2 (S2). Estimation methods of the parameters: measured (M), calibrated (C) and regression (R)

Name	Model	Signification	Unit	Method	Station	S1	S2
A_{DEEP}	Groundwater	Surface of the recharge area	km^2	M	–	3	
SAWC		Soil available water capacity	mm	M	–	105	
K_c		Coefficient of vegetation	–	M	–	0.777/0.955	
Rf_{coeff}		Runoff coefficient	–	M	–	0.128	
$Overflow_d$		Maximum hydraulic head due to deep reservoir overflow	m	C	–	0.12	0.10
k_d		Reservoir recession coefficient	–	C	–	0.02	0.03
$A_{PERCHED}$		Surface of the recharge area	km^2	M	–	0.05	
$Overflow_p$		Maximum hydraulic head due to perched reservoir overflow	m	C	–	0.09	0.06
k_p		Reservoir recession coefficient	day^{-1}	C	–	0.06	0.11
α		Trigger coefficient between WL_p and WL_d expressed as the contribution of WL_p	–	C	–	0.30	0.23
HT	Landslide creep	Hydraulic threshold	–	C	–	−0.19	−0.20
β		Rock weakening coefficient	–	C	A13	$8.22\ 10^{-4}$	$1.20\ 10^{-3}$
					A16	$5.34\ 10^{-4}$	$7.01\ 10^{-4}$
					1101	$1.19\ 10^{-3}$	$1.51\ 10^{-3}$
γ		Rock strengthening coefficient	mm	C	A13	$5.71\ 10^{-4}$	$9.72\ 10^{-4}$
					A16	$1.65\ 10^{-8}$	$2.44\ 10^{-4}$
					1101	$1.09\ 10^{-3}$	$1.28\ 10^{-3}$
a	Time-series	Triggering coefficient of WL_C	–	R	A13	0.30	0.37
					A16	0.35	0.44
					1101	0.33	0.44
b		Rock weakening impact coefficient	–	R	–	1	1
c		Initial state of the modelled trend	mm	R	A13	−0.44	−0.28
					A16	−0.19	−0.21
					1101	0.02	0.27

et al. 2010; Huang et al. 2012). The model structure presented in Fig. 1 respects this feature and is based on a two-layer reservoir constituted of a perched aquifer and of a deep aquifer.

The deep aquifer is considered to be recharged by a large area at the scale of the massif (A_{DEEP}, [L^2]), whereas the recharge of the perched aquifer is located on the landslide area ($A_{PERCHED}$, [L^2]). The input of the perched aquifer is considered as equal to raw precipitation because the unstable area is characterised by a high infiltration rate of localised recharge in the collapse zone through bare ground, crevices or counter-slopes (Cappa et al. 2004; Charlier et al. 2010) where evapotranspiration becomes a negligible process. The deep aquifer is recharged by percolation from the perched aquifer in the landslide area and by diffuse infiltration from a soil reservoir in the rest of the massif. Lastly, since groundwater is drained by temporary streams and springs during high water periods, overflow processes are taken into account, adding overflow thresholds to both perched and deep aquifer reservoirs ($Overflow_p$ and $Overflow_d$, [L]).

Each reservoir has an input H_{in} and an output H_{out}. The depth H of water stored in the reservoir is obtained using the following equation:

$$\frac{dH}{dt} = H_{in} - H_{out} \text{ with } H_{out} = k \cdot H \quad (3)$$

where k ([T^{-1}] dimension) is a constant characterising the recession curve of the reservoir (k_p for perched reservoirs and k_d for deep reservoirs).

The soil reservoir is a soil-water balance model which simulates a diffuse groundwater recharge through soil cover according to the workflow calculation proposed by Vallet et al. (2015a). This computation requires a precipitation dataset and the estimation of the evapotranspiration ET ([L] dimension) and of parameters characterising the recharge area. ET is estimated with a calibrated temperature-based evapotranspiration equation (Penman-

Monteith reduced set, Allen et al. 1998) coupled with a vegetation coefficient K_c [dimensionless]. The determination of the parameters of the recharge area (soil available water capacity SAWC [L], the K_c and the surface runoff Rf_{coeff} [dimensionless]) is based on a spatial analysis requiring field observations (soil, vegetation and geological survey….) and spatial datasets (digital elevation models, aerial photographs and geological maps).

The hydro-mechanical study of Cappa et al. (2014) showed that the deep aquifer water pressure, beneath the unstable zone, can facilitate the rupture of slow-moving landslides as a result of stress transfer and of frictional weakening. In addition to the perched aquifer, the deep aquifer is assumed to possibly trigger the displacement of the deep-seated landslide. A composite groundwater level WL_c [dimensionless] triggering the landside destabilisation is estimated from both perched and deep reservoir water levels (WL_p [L] and WL_d [L] according to a triggering coefficient α varying from 1 to 0 (Fig. 1, Eq. (4)). WL_c is deduced from standardised water levels (i.e. standard score) of the perched and the deep reservoirs in order to be independent of the water level amplitudes.

$$WL_c = \alpha WL_p + (1-\alpha)WL_d \quad (4)$$

The adjustment of the alpha parameter during the calibration phase is constrained by the measured data and will therefore inform about the influence or importance of the deep aquifer on the destabilisation (alpha=1 means that the deep aquifer does not play any role; conversely, alpha=0 means that the deep aquifer entirely controls the destabilisation).

Landslide creep model: long-term displacement trend

The design of landslide creep model is inspired by two main concepts deduced from two standard mechanical tests: the creep test and the fatigue test. First, in the creep test, a time-dependent deformation of a solid material occurs under an applied stress. Although the applied stress is constant, the strain rate exponentially increases with strain, eventually leading to fracture. This evolution is referred to as the rock weakening process. The GLIDE model therefore non-linearly links stress and strain. Second, in the fatigue test, the progressive and localised structural damage of a solid material occurs under a cyclic applied stress. The input oscillatory stress can be assimilated to the seasonal groundwater pressure variations (low-cycle fatigue). However, the stress amplitude has to be above a threshold named "fatigue limit" in order to produce the failure of the material after a given number of cycles. Below this threshold, an infinite number of cycles can occur without affecting the material (no failure). Therefore, the GLIDE model includes a threshold which has to be overtaken in order to produce rock weakening.

As this study focuses on rainfall-induced landslides, the pore water pressure is considered as being the only stress which induces destabilisation since the weight of the landslide body is not yet sufficient to self-destabilise the landslide. The threshold is thus linked to the groundwater level of the aquifer(s) controlling the destabilisation. This is confirmed for example by the Vaiont case, where the inverse velocity method (Fukuzono 1985), which neglects triggering factors such as pore water pressure, considers that the landslide destabilisation kinematics is self-sufficient and will follow a known empirical law. However, in the case of the Vaiont landslide, this method would have led to two false failure alerts (1960 and 1962) as the landslide displacement velocity fell sharply, after a typical creep tertiary curve, once the water level in the dam lake had decreased (Petley and Petley 2006). Therefore, for the Vaiont landslide, the control of the creep curve by the groundwater level could be relevant.

The GLIDE lumped model approximates the creep behaviour of the Séchilienne landslide as a homogeneous entity named "Landslide creep model". It does not allow to relate the lumped parameters to specific physical processes inside the landslide. Consequently, the model remains global about the landslide physics behind the model, and the significance of the lumped parameters remains conceptual. The GLIDE model is based on the physical concept in which weakening and consolidation are two antagonist processes. Consolidation and weakening can occur at the same time at different landslide locations, but the GLIDE model will only consider the result of these processes. If weakening overcomes consolidation, the GLIDE model should simulate the resulting weakening. Conversely, if consolidation overcomes weakening, the GLIDE model should simulate the resulting consolidation.

The long-term displacement trend observed on creeping landslides is a direct consequence of the time evolution of the whole landslide strength. Thus, the modelled creep trend MCT ([L] dimension) increases with the whole landslide weakening, whereas the MCT decreases with the landslide consolidation. The composite water level WL_c output from the groundwater model is considered as the water pressure input of the landslide creep model. The landslide creep model is based on a constant hydraulic threshold HT (dimensionless) which has to be exceeded (WL_c>HT) in order to increase the MCT, thus simulating rock weakening. Conversely, when the WL_c does not reach the hydraulic threshold, the MCT decreases, simulating rock consolidation. The weakening mechanism is assumed to be proportional to the water level exceeding the hydraulic threshold (WL_c−HT) by adjusting a weakening coefficient β (dimensionless). The weakening process depends on the antecedent rock mass strength:

$$MCT_{j+1} = MCT_j + MCT_j\beta(WL_c - HT) \quad (5)$$

with MCT_j and MCT_{j+1} respectively stand for MCT at day j and day j+1. On the other hand, the landslide consolidation process is assumed not to be proportional to the groundwater level and not to depend on the antecedent rock mass strength. The consolidation is estimated by subtracting a strengthening coefficient γ ([L] dimension) to MCT:

$$MCT_{j+1} = MCT_j - \gamma \quad (6)$$

Time-series model: displacement re-composition

The time-series model combines the results of both the groundwater model and the landslide creep model. First, the modelled detrended displacement MDD (dimensionless) is assumed to be linearly proportional to the WL_c output of the groundwater model (Eq. (7)). This assumption is based on Vallet et al. (2015a) which show that the coefficient of determination obtained from a linear regression between an estimated water-level and the seasonal

variation of landslide velocity is really high (>0.6), confirming that a linear relationship between the two variables should allow to well simulate the variability of the displacement time-series based on a water level.

$$\mathrm{MDD} = a\,\mathrm{WL_c} + 1 \tag{7}$$

The a parameter (dimensionless) is considered as the triggering impact of the water level on the landslide destabilisation. A shifting intercept is set to 1 since the detrended component fluctuates around 1, whereas $\mathrm{WL_c}$ fluctuates around 0 as a consequence of the water level normalisation.

Second, the modelled displacement trend MDT ([L] dimension) is assumed to be proportional to the MCT state output of the landslide creep model (b parameter (dimensionless)) of which a shifting c parameter ([L] dimension), accounting for the initial condition of the MCT, is added as follows:

$$\mathrm{MDT} = b\,\mathrm{MCT} + c \tag{8}$$

The modelled displacement MD ([L] dimension) is then reconstructed by multiplying MDD and MDT which gives:

$$\begin{aligned}\mathrm{MD} &= (b\,\mathrm{MCT} + c)(a\,\mathrm{WL_c} + 1)\\ &= ab\,\mathrm{MCT}\,\mathrm{WL_c} + b\,\mathrm{MCT} + ac\,\mathrm{WL_c} + c\end{aligned} \tag{9}$$

Equation (9) can be simplified as follows:

$$\mathrm{MD} = A\,\mathrm{MCT}\,\mathrm{WL_c} + B\,\mathrm{MCT} + C\,\mathrm{WL_c} + D \tag{10}$$

Equation (10) represents the governing equation of the time-series model at the conditions that the A, B, C and D coefficients verify the equality $AB^{-1}=CD^{-1}$ (compare Eq. (9) and Eq. (10) for the link between a, b, c and A, B, C, D).

Parameterization and calibration strategy of the model

Model parameters

Modelling the displacement at one station using the GLIDE model requires 16 parameters (Table 1). In order to limit the equifinality, that is the fact that acceptable simulations can be reached by many potential sets of parameterization (Beven 2006), five parameters are estimated and three parameters are deduced from multiple linear regressions (Table 1). Consequently, the GLIDE model requires the calibration of the other eight parameters, that is an acceptable parameterization strategy for such reservoir models, considering that GLIDE is able to simulate two outputs (groundwater level and creep trend).

The groundwater model needs a total of 10 parameters (A_{DEEP}, SAWC, K_c, $\mathrm{Rf_{coeff}}$, $\mathrm{Overflow_d}$, k_d, A_{PERCHED}, $\mathrm{Overflow_p}$, k_p, α) of which five (A_{DEEP}, SAWC, K_c, $\mathrm{Rf_{coeff}}$, A_{PERCHED}) can be estimated from field investigations and five are calibrated. Additionally, the groundwater model also needs three initial conditions of the soil, the perched reservoir and the deep reservoir. The landslide creep model needs a total of three parameters (HT, β, γ) which should be calibrated. The landslide creep model also needs an initial condition for the MCT. This initial value of MCT is set to 1 since the adjustment of the MCT initial condition is carried out by the calibration of the coefficient c pertaining to the time-series model. Because the GLIDE model just takes into account the possible variations of the rock mechanical properties but not those of the hydraulic properties, the recession coefficient and the HT threshold do not depend on the landslide deformation state.

The three parameters (a, b and c) of the time-series model are determined with a constraint multiple linear regression between the three inputs of the time-series model ($\mathrm{MCT}\times\mathrm{WL_c}$, MCT and $\mathrm{WL_c}$) and the measured displacement output, provided that the coefficients (A, B, C and D) of Eq. (10) verify the equality $AB^{-1}=CD^{-1}$. The use of a multiple linear regression allows to avoid the integration of a, b and c from Eqs. (7) and (8) into the calibration process.

The case of modelling multiple displacement records

In case of modelling displacement records of multiple stations, the modularity of the model allows adjustment in order to take into account spatial variability. Various strategies may be performed depending on the variability of the landslide behaviour.

Calibration strategy of the groundwater model with regard to the detrended component In the case of homogeneous detrended displacement over various measurement sites, the groundwater model can then be assumed to be representative of the whole landslide, leading to use the groundwater model as lumped at the landslide scale. In the opposite case, the groundwater level triggering the landslide destabilisation should be considered to vary according to the station location. In this case, a shift lag has to be introduced in the groundwater model for each zone having significant detrended component behaviour. The HT threshold, although belonging to the landslide creep model, is considered as dependent of the groundwater conditions and not of the landslide deformation. Therefore, the HT threshold parameter has been chosen to be calibrated in function of the detrended component behaviour. Indeed, the spatial variability of the landslide response to groundwater fluctuation is taken into account by the β and γ parameters, and the HT threshold parameter is mainly linked to the groundwater level variations. In the case of homogeneous detrended displacement over various measurement sites, the HT threshold is kept identical for the whole landslide and conversely.

Calibration strategy of the landslide creep model with regard to the trend component In the case of a displacement trend following the same increasing pattern at various measurement sites, the landslide creep model can be considered to be representative of the landslide and only the a, b and c parameters of the time-series model have to be estimated with a multiple regression. In the opposite case, the parameters of the landslide creep model (except HT parameter) and of the time-series model have to be calibrated separately for each station. In that case, the MCT output of the landslide creep model is equal to the displacement trend of each station and only the c parameter has to be estimated. The b parameter is therefore equal to 1 and constraints of Eq. (10) become B=1 and $A=CD^{-1}$. Lastly, for landslides where no trend can be identified, only the groundwater model is necessary to simulate the displacement.

Calibration periods and optimization

Simulated annealing (Kirkpatrick et al. 1983; Černý 1985) is a probabilistic optimization method which allows to find an approximate value of the global minimum of a cost function that may

possess several local minima. Simulated annealing is a generally applicable, easy-to-implement and computationally cost-reasonable algorithm adapted for large search spaces (Bertsimas and Tsitsiklis 1993). In addition, this method is able to produce good solutions independently of the optimization structure problem. It is implemented here to calibrate the GLIDE model. It allows a fully automatic and optimal optimization process of the model parameters.

The displacement trend accentuates the calibration at the end of the interval where amplitudes are higher than average, leading to an unbalanced calibration. A consequence of this accentuation implies that recent periods are better simulated than former ones. In order to disregard the trend influence on the calibration process, the model is calibrated only on the detrended component by removing the modelled trend from the measured and modelled displacements. Moreover, because of the long-term trend, a simple classical partition of the time-series dataset into two distinct and successive periods (a calibration period and a validation period) appears to be inappropriate to account for the time-dependent evolution of the data. Thus, the definition of the calibration and validation periods is defined differently. The time-series is split into constant length intervals which are alternately assigned to the calibration and to the validation intervals. This setup allows to obtain both the calibration and the validation intervals spread on the entire variation range. Lastly, to limit the influence of such partitioning as well as to assess the model performance on the whole time-series, a split sample test is conducted (Klemeš 1986). This test consists in considering calibration scenarios (scenario 1 and 2) corresponding to reversed sets of calibration periods.

Performance criteria

Three criteria were used to assess the model performances: the Nash-Sutcliffe coefficient of efficiency NS (Nash and Sutcliffe 1970, Eq. (11)), the Nash-Sutcliffe with logarithmic values NSL (Krause et al. 2005) and the root mean square error (RMSE, Eq. (12)). The NSL indicator corresponds to the NS coefficient calculated with logarithmic values of observed (O) or predicted (P) in Eq. (11).

$$\mathrm{NS} = 1 - \frac{\sum_{i=1}^{n} (O_i - P_i)^2}{\sum_{i=1}^{n} \left(O_i - \overline{O}\right)^2} \tag{11}$$

$$\mathrm{RMSE} = \sqrt{\frac{\sum_{i=1}^{n} (O_i - P_i)^2}{n}} \tag{12}$$

where i is an index representing the time step ($1<i<n$); n, the number of time steps in the time-series, with O for observed values ($\overline{O}$ being the mean of the observed values) and P for predicted values.

The ranges of NS and NSL are between 1.0 (perfect fit) and $-\infty$. A negative value indicates that the mean of the observed time-series is a better predictor than the model. The RMSE criteria range between 0 and $+\infty$, with 0 signifying a perfect fit. The NS and the RMSE criteria are sensitive to extreme values, while the NSL allows to give more weight to low values. In the case of modelling multiple displacement measurement stations, calibration with a unique composite performance indicator simplifies the calibration strategy. Rather than computing a performance criterion of each type for each station, a unique weighted mean of the performance criteria ($\mathrm{NS_m}$, $\mathrm{NSL_m}$ and $\mathrm{RMSE_m}$) is calculated. This calculation is proportional to the dataset time extent of each station. The $\mathrm{NS_m}$, the $\mathrm{NSL_m}$ and the $\mathrm{RMSE_m}$ criteria are used to assess the performance for the detrended displacement (groundwater model), whereas the $\mathrm{RMSE_m}$ indicator is only used for the two other components (landslide creep model and time-series model). Indeed, NS and NSL indicator values depend on the time-series mean and are therefore biased by the long-term trend. The calibration of the GLIDE model parameters with the simulated annealing optimization method is based on the $\mathrm{NS_m}$ criterion.

Study site: the Séchilienne landslide

Geological context and landslide description

The Séchilienne landslide is located in the southwestern part of the Belledonne External Crystalline Massif (western Alps) on the southern slope of the Mont Sec (Fig. 2). The Belledone Massif, which extends over more than 120 km in a N30° direction with an altitude of 3000 m a.s.l., is bounded to the west by the large depression of the Isère valley (Fig. 2a). The Belledone Massif consists of a complex of varied Palaeozoic metamorphic rocks (Ménot 1988; Le Roux et al. 2011). These metamorphic rocks are unconformably covered by Mesozoic sedimentary rocks (Carboniferous and Triassic-Liassic on Fig. 2a) and were reworked during the Alpine orogenesis.

The massif is divided into two major tectonic and lithological domains: the external domain to the west and the internal one to the east (Guillot et al. 2009). These two domains are separated by the major Late Paleozoic near-vertical NNE-trending Belledonne Middle Fault (Fig. 2a). To the west, the external domain consists of micaschists unconformably covered with Carboniferous and Mesozoic (Triassic-Liassic) sedimentary rocks and Quaternary deposits (Le Roux et al. 2011; Fig. 2a). The Romanche valley morphology results from the alternate activity of water and ice during Quaternary times (Monjuvent and Winistörfer 1980; Le Roux et al. 2011; Moraine on Fig. 2a).

Landslide geological structure

Recent dating of Le Roux (2009) by the method of cosmogenic isotopes performed on the Séchilienne landslide shows that slope destabilisation was not an immediate consequence of the Romanche valley debutressing but occurred over 5400 years after ice down-wastage in the valleys (Lebrouc et al. 2013). Lebrouc et al. (2013) suggest that this time lag can be explained by the persistence of permafrost, which would have temporarily increased the resistance of the slope.

The Séchilienne landslide is limited eastwards by a N-S fault scarp and northwards, below the Mont Sec, by a major head scarp of several hundred meters wide and several tens of meters high. Rare geomorphological evidence allows to precisely define the western and southern boundaries of the unstable area. Below the head scarp, between 1100 and 950 m a.s.l., a gentle slope zone is in depletion, while between 950 and 450 m a.s.l., the slope becomes steeper (more than 40°) and is interpreted as an accumulation zone (Vengeon 1998; Le Roux et al. 2011). The area affected by the landslide is estimated to about 1 km² (Le Roux 2009). The slope is cut by a dense network of two sets of near-vertical open fractures trending N110° to N120° and N70° (Le Roux et al. 2011; Fig. 2a, b). In the accumulation zone, the dense network of opened N70°

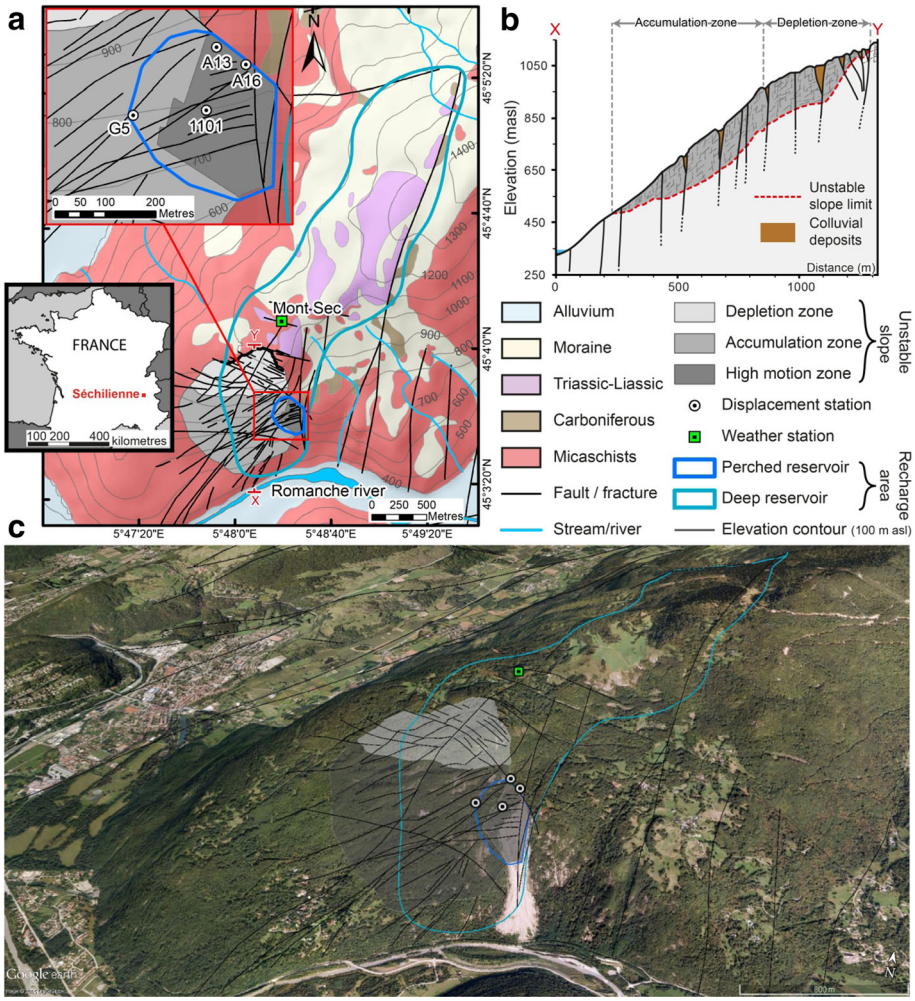

Fig. 2 Séchilienne landslide site and monitoring network. **a** Localisation and geological map of the southern part of Belledonne massif with faults network within the Séchilienne landslide. **b** Cross section along the Séchilienne landslide. The "unstable slope limit" refer to the part of the slope where the porosity exceeds a threshold porosity of 3.7 % (Le Roux et al. 2011). **c** 3D view of the Séchilienne massif where faults and network are displayed

fractures divides the slope into several vertical compartments. The fractures are filled by colluvium and by clayey material near the surface, and change to crushed zones filled with clayed material in depth (Vengeon 1998; Lebrouc et al. 2013). Additionally, a large number of N50°–N70° fractures dipping near-parallel to the slope are present in the accumulation zone (Vengeon 1998). In the upper part of the slope (depletion zone), the N110° to N120° fractures are dominant (Lebrouc et al. 2013; Fig. 2a, c).

Kinematic and deformation

The Séchilienne landslide is presently the most active gravitational movement at the present time in the area (Duranthon et al. 2003). The displacement monitoring shows displacement vectors relatively homogeneous in directions (N140°) and in dip angles (10° to 20°). Low velocity displacements (2 to 15 cm/year) are observed for the depletion and the accumulation zones (Le Roux et al. 2011). These velocities gradually decrease towards the west and south, allowing to define the limits of the unstable area. The unstable mass is estimated between 48 and 63 million m^3 (Le Roux et al. 2011). A very active moving zone, where displacement velocities about 150 cm/year are measured, lies within the unstable slope. This zone is responsible for abundant rockfall and its volume is estimated at 3 million m^3 (Le Roux et al. 2011). Seismic and electrical tomographic profiles allow to characterise the micaschists mass deconsolidation state (Le Roux et al. 2011). The zones strongly affected by the landslide (depletion zone and high motion zone) result from an intense fracturing and air-filled voids (Le Roux et al. 2011).

The Séchilienne landslide is characterised by a deep progressive deformation controlled by the network of faults and fractures. A particularity of the Séchilienne landslide seems to be the absence of a well-defined basal sliding surface. The landslide is affected by a deeply rooted (about 100–150 m) toppling movement of the N50° to 70° slabs to the valley (accumulation zone) coupled with the sagging of the upper slope (depletion zone) beneath the Mont Sec (Vengeon 1998; Durville et al. 2009; Lebrouc et al. 2013).

Hydro-mechanical background

The Séchilienne site is characterised by a mountain climate where precipitations consist of rain and snow. Annual snow amount is 7-fold lower than rainfall. Unlike the groundwater recharge which shows high seasonal contrasts (dry summers vs. wet

winters), precipitations do not show any pronounced seasonal tendencies.

The Séchilienne landslide shows a higher hydraulic conductivity than the underlying stable bedrock (Vengeon 1998; Meric et al. 2005; Le Roux et al. 2011). This vertical heterogeneity leads to a two-layer aquifer, with a shallow perched aquifer localised in the unstable zone and a deep aquifer in the whole massif overlaid by a thick (about 100 m) vadose zone (Guglielmi et al. 2002). Heterogeneous, anisotropic and discontinuous properties of the landslide lead to a discontinuous perched fractured reservoir. The massif supporting the Séchilienne landslide is characterised by a dual-permeability behaviour typical of fractured rock aquifers where conductive fractures play a major role in the drainage (Vallet et al. 2015b). In addition, the sedimentary deposits distributed above the landslide (Fig. 2a) hold a perched aquifer (Guglielmi et al. 2002).

The perched aquifer in the landslide is temporary, mainly discontinuous, and its extent and connectivity fluctuate according to short-term recharge variations (Vallet et al. 2015b). The recharge of the landslide-perched aquifer is essentially local, enhanced by the trenches and the counterscarps which tend to limit the runoff and to facilitate groundwater infiltration in the landslide area. However, during high-flow periods, the recharge area of the landslide-perched aquifer may become larger than the landslide surface and may include the remote sedimentary cover-perched aquifer (Guglielmi et al. 2002; Vallet et al. 2015b).

The hydro-mechanical study of Cappa et al. (2014) shows that the deep aquifer can trigger the Séchilienne landslide destabilisation. The Séchilienne landslide destabilisation can therefore be regarded as triggered by a dual-aquifer layer: the landslide-perched aquifer and the deep aquifer. Consequently, the Séchilienne landslide is characterised by a good correlation between antecedent precipitation and average displacements (Rochet et al. 1994; Alfonsi 1997; Durville et al. 2009; Chanut et al. 2013; Vallet et al. 2015a).

Dataset

Measured meteorological and displacement data

Precipitations are recorded at the Mont Sec weather station, located a few hundred meters above the disturbed zone (Fig. 2). This station is equipped with rain and snow gauges. The snow gauge provides an estimate of the snowpack thickness expressed in water depth. The equivalence between the snowpack thickness and the water depth is estimated with the measurement of the attenuation of the cosmic radiation by the snowpack. Therefore, this station allows to account for snow storage and melting which cause the infiltration at different rates and with different time delays between rain and snow. As a consequence, hereafter, precipitation combines rainfall and snow melt as one component. The Séchilienne landslide is monitored by several displacement measurement stations, managed by the CERE MA Lyon (Duranthon et al. 2003). A variety of techniques (extensometers, radar, infra-red, inclinometers and GPS) is used. The aim of this study is to assess short-term to long-term influences of precipitation on landslide displacement velocities. We focused on displacement measurement stations which were installed since the very beginning of the Séchilienne monitoring, thus maximising the extents of the time-series data. For this reason, only the data from one infra-red measurement station (referred to as 1101) and from three extensometers (referred to as A16, A13 and G5) have been used. 1101, A16 and A13 are located within the most active unstable zone (Fig. 2). Data are available from 1 September 1992 to 31 August 2013 with record percentages of 87 % for A16, 94 % for A13, 33 % for 1101, 45 % for G5 and 100 % for the weather station (Table 2). The extensometers used at Séchilienne are characterised by measurement errors of ±0.5 mm, while infra-red measurement errors are ±4 mm. Although the difference between the two errors seems important, it should not affect the results since the displacement data are filtered and the frequencies below 8 days are not considered.

Data processing

The groundwater recharge is estimated according to the workflow calculation proposed by Vallet et al. (2015a). Parameters of the recharge area were estimated by Vallet et al. (2015a) as follows: a SAWC of 105 mm, an Rf_{coeff} of 12.8 % and a K_c varying linearly from 0.777 in winter to 0.955 in summer. Displacement time-series show outliers attributed either to instrumentation error or to external influencing factors. For example, extensometer stations are, among others, influenced by sticky snow, strong winds, fallen branches and electromagnetic interferences. Infra-red measurements are recorded only during good weather conditions and if no obstacle, such as branches, hinders the measurements. A method has been developed to remove the largest outliers from the displacement data. In this method, the displacement values are considered as unacceptable outliers when their values exceed a given threshold. The threshold is defined with the help of the computed standard deviation and the computed mean of displacement data included in a moving window. The threshold is further arbitrarily adjusted according to the signal characteristics. The arbitrary adjustment factor is chosen after performing several iterative tests and by retaining the factor which best eliminates the visually identified outliers. The threshold definition is obtained by adding or subtracting the mean to the product of the standard deviation by the arbitrary factor (threshold=mean±(standard deviation×arbitrary factor)). Two successive windows are used: an annual window (365 days) and a seasonal window (90 days). The aim of the wavelet analysis is to investigate the precipitation and recharge influences on the displacement from short-time to long-time scales. Since recharge dynamics occurred mostly in the monthly to seasonal frequency domain, high frequencies corresponding to 1 to 8 days of displacement measurement periods were removed using multi-resolution, to remove signal noise. Meteorological and displacement datasets are hereafter investigated at a computation step of 8 days. An example of data filtering using multi-resolution and outliers removing for the A13 extensometer is shown in Fig. 3.

The multiplicative method is the more appropriate method to decompose the displacement time-series (detail in the "Statistical time-series decomposition" section). The displacement trend is defined by curve fitting of a fifth-order polynomial (parametric trend) for the four displacement measurement stations. A fifth-order polynomial is used because it maintains the balance between under-fitting and over-fitting with the displacement dataset, thus allowing to faithfully reproduce the trend. The result is a unitless time-series fluctuating around 1, named detrended displacement, with both variance and mean trend removed (Fig. 4). Since the trend amplitude in the raw displacement signal tends to hide

Table 2 Summary of the meteorological and landslide velocity dataset

Name	Type	From	To	Number of data (days)
A13	Extensometer	01 September 1992	31 August 2013	7182
A16	Extensometer	02 March 1994	30 June 2013	6685
1101	Infra-red	01 January 2006	30 June 2013	2519
G5	Extensometer	15 September 2000	8 July 2013	3614
Mont Sec	Weather station	01 September 1992	31 August 2013	7671

variations at seasonal and annual scales, both raw and detrended displacement signals were compared in the wavelet analysis.

Model parameterization for the case study

The GLIDE model is calibrated against the displacement measurement stations located on the most active zone (1101, A16 and A13). The data of the G5 extensometer are disregarded because they are characterised by a low signal-to-noise ratio (Fig. 4). The model calibration is implemented according to the results detailed in the "Discussion of the groundwater functioning and modelling constraints" section. The similarity of the detrended displacements of the four stations leads to use the groundwater lumped model without introducing any shift lag. The different trends observed between the four stations lead to separately calibrate the parameters of the landslide creep model and the time-series model for each station. For the groundwater model, the soil reservoir parameters are detailed in the "Data processing" section. The recharge areas of the deep aquifer (identical to that of the soil reservoir) and of the perched aquifer are estimated to 3 km^2 and 0.05 km^2, respectively (Fig. 2), according to Guglielmi et al. (2002) and Vallet et al. (2015b). The recharge area of the perched aquifer is limited to the high motion zone of the landslide.

In this study, three displacement time-series are modelled, involving 23 parameters. Five parameters are deduced from field measurements, 12 parameters are calibrated and 6 are deduced from multiple linear regressions. Among these parameters, 11 parameters are common to the three stations (the 10 parameters of the groundwater model and 1 parameter (HT) of the landslide creep model) and 12 parameters are specific to the targeted station (4 parameters per station of which 2 are deduced from the multiple linear regression). A warm-up period of 1 year is implemented, after which the model output variables can be considered as independent from the initialisation bias. Initial conditions of the warm-up period for the soil, perched and the deep reservoir are set by default at 50 % of SAWC maximum, $Overflow_p$ and $Overflow_d$, respectively. The groundwater model requires five parameters (k_p, K_c, $Overflow_p$, $Overflow_d$ and α) to be calibrated. The landslide creep model HT parameter remains the same for the three targeted stations, while the β and γ parameters, accounting for local variabilities, are calibrated specifically. Similarly, the time-series model parameters (a, c) are deduced from the multiple linear regression for each target station. At Séchilienne, the b parameter is equal to 1 (see "The case of modelling multiple displacement records" section).

The performances of the numerical model are analysed with a sensitivity analysis of the performance indicators from week (8 days, minimum imposed by the use of displacement data filtered at 8 days) to month (31 days) time step windows. Two-year periods were alternatively assigned to the calibration and to the validation intervals.

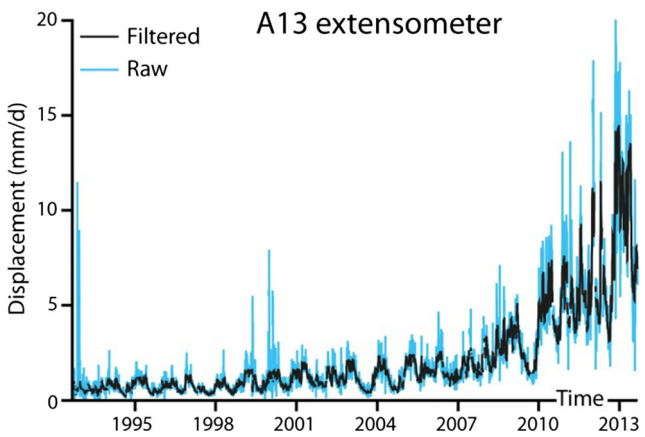

Fig. 3 Displacement data processing: multi-resolution filtering and outlier removing (see "Data processing" section) on the A13 extensometer data

Results and discussions

Investigation of hydro-mechanical processes using wavelet analysis

Hydrologic input

Precipitation and estimated recharge time-series are plotted in Fig. 4. Precipitations show low seasonal variations with winter and summer months drier than the rest of the year likely due to water storage in the form of snow cover. On the contrary, the recharge signal shows a high seasonal contrast (dry summer vs. wet winter). The recharge signal is clearly influenced by atmospheric temperature variations through evapotranspiration processes. The precipitation and the recharge signals do not show any trend, and the amplitude of the seasonal variations remains constant over the whole time-series.

The CWT of precipitation plotted in Fig. 5a shows numerous weekly to monthly structures (less than 64 days) mostly during winter periods. Some abnormally wet years even show consistent seasonal structures (64–128 days period) during the 1994, 1995, 1999, 2002, 2005, 2008, 2011 and 2012 winters. One-year structures can be identified from 2002 to 2004 and from 2008 to 2010, which are the years with the highest monthly rainfall depth. Lastly, a 5-year component is observed, reflecting a clear variation in large-scale precipitation distribution. The CWT of recharge (Fig. 5b) is similar to that of precipitation, but structures almost miss during summer months. It leads to a more pronounced power contrast in the scalogram, generating spread structures. Moreover, 1-year structures for recharge, matching with wetter years, are more

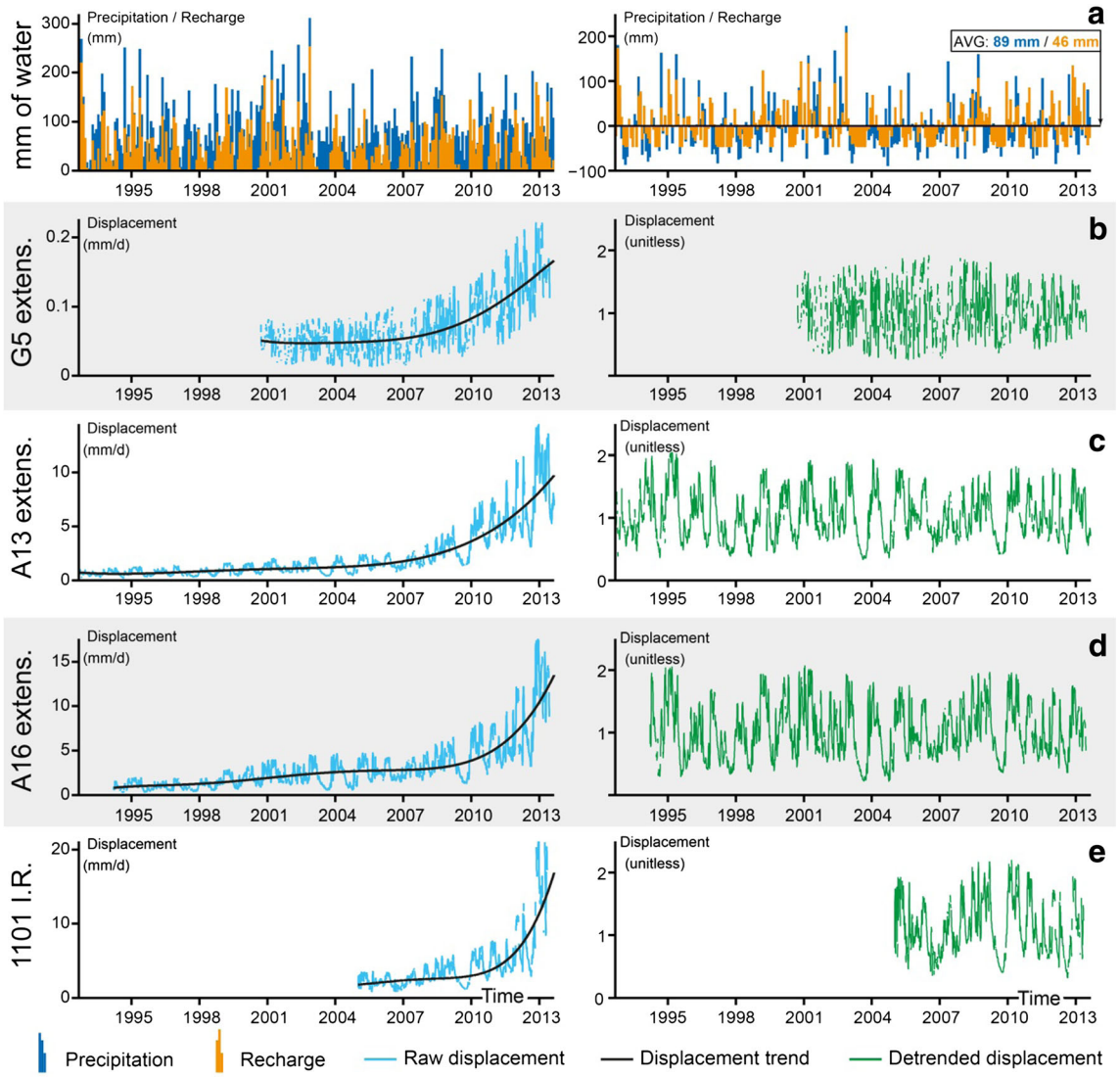

Fig. 4 Input and output dataset. **a** Input: monthly precipitation and monthly recharge. **b–e** Output: filtered displacement data with raw signal and trend and detrended signal

developed and more regular over the time-series than those for precipitation signal.

Displacement velocity output

Long-term displacement time-series, plotted in Fig. 4, show that displacement rates and amplitudes increase significantly with time from 2008 onwards. The displacement time-series show an exponential growth, with the amplitude of the infra-annual variations growing with the mean of the series. Although the G5 extensometer is located in a less active zone, the trend is also observable, meaning that the creep process affects the whole landslide. However, the trends observed at the four displacement measurement stations have a significantly different increasing pattern (Fig. 4). The detrended displacement time-series of the four displacement measurement stations show sharp seasonal variations with the lowest values in summer and the highest values in winter (Fig. 4), within a relatively constant range of values over the years. The seasonal variations of the four stations show synchronous peaks and troughs, meaning that the hydro-mechanical response at the infra-annual scale is homogeneous over the most active zone of the landslide.

Since the four displacement data series show similar patterns and since A13 has the widest recording period, results of the wavelet analysis are presented only for the extensometer A13. The CWT for A13 is performed for the raw displacement and for the detrended displacement (Fig. 5c, d). The CWT of A13 raw displacement (Fig. 5c) shows a weak power at all scales until 2008. From 2010 to 2013, high-frequency structures (<64 days period) gradually increase in number, in power and in period. A vertical "dendriform" structure in the scalogram for an 8-day to a 1-year period is observed, highlighting the multi-scale distribution of the power through scales over the more recent years. This scale effect reveals that the landslide destabilisation at the annual scale may be linked to the destabilisation at lower periods. The CWT of the detrended displacement of A13 (Fig. 5d) shows a very different scalogram. Low-power erratic structures are observed at the infra-annual scale, whereas most of the power is located at the annual scale through regular structures which appear concomitant with those highlighted in the recharge signal.

Landslide input-output relationships

Relationships between the various signals are investigated using XWT and WTC. Figure 6 presents cross-scalograms between precipitations and recharge (input signals) and detrended displacements (output signal). The XWT between precipitation and detrended displacement (Fig. 6a) highlights numerous weekly to seasonal structures (8–128-day period) that are irregularly connected through scales and erratically distributed through time. Compared with CWT of precipitations and recharge signals (Fig. 5a, b), the occurrence of these structures matches with highest water inputs. A discontinuous structure on the 1-year band (256–512-day period) is also displayed. Unlike for infra-seasonal structures, no significant coherence is observed for annual structures on the WTC although XWT shows high power. This analysis shows that precipitations and displacements are correlated in the infra-annual scale only, scale at which the power for the displacement signal is the lowest, meaning that the precipitation signal is not the variable able to explain most of the displacement variations. XWT between recharge and detrended displacement (Fig. 6b) shows identical coherent structures in the infra-annual scale. However, structures in the 1-year band are more widespread and more connected. A significant coherence appears throughout the time-scale space from 8 days to 2 years, suggesting strong relationships between recharge and detrended displacement time-series at small and large scales (except at pluri-annual scales such as the 5-year band visible on the CWT). It shows globally that the recharge signal is correlated to displacements over the whole time-frequency space from weekly to bi-annual scales.

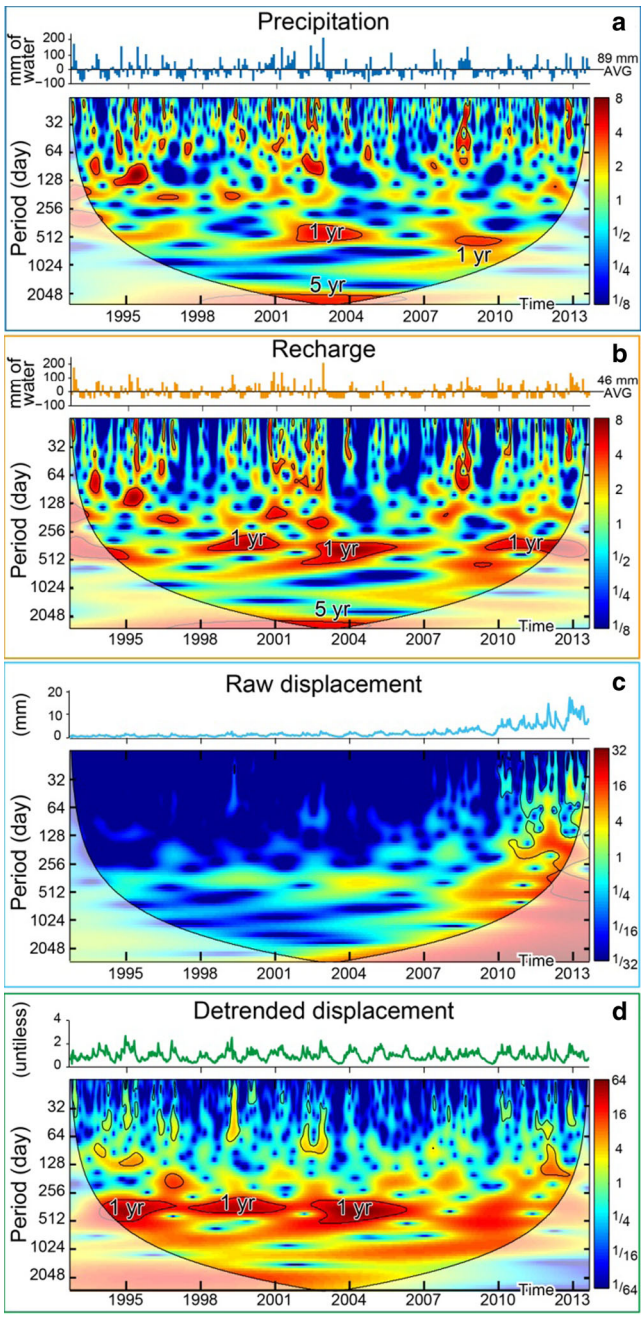

Fig. 5 Continuous wavelet power spectra of **a** precipitation, **b** recharge, **c** A13 raw displacement and **d** A13 detrended displacement. The *thick black line* designates the 5 % significance level against red noise. The cone of influence, whose edge effects might distort the picture, is shown by using attenuated colour intensities

Discussion of the groundwater functioning and modelling constraints

The analysis of the input-output relationships shows that annual variations of the detrended displacement are better explained by the recharge signal than by the precipitation signal. It appears that the infra-annual detrended displacement results in high precipitation events (for both precipitation and recharge signals), whereas annual and bi-annual variations, for which most of the variability is observed, are rather linked to recharge and thus to groundwater processes. Consequently, we may assume that two recharge types occur. The periodic variations of the Séchilienne displacement seem to be triggered by a dual-groundwater layer with a perched (reactive aquifer responsible of high-frequency displacements) and a deep aquifer (inertial aquifer responsible of low frequencies of displacement). This assumption is in agreement with Cappa et al. (2014) which show that pore pressure effects in the deep aquifer can resolve at least 40 % of the total motions measured at the slope surface, which is far from being negligible. In addition, the hydrochemistry survey of Vallet et al. (2015b) shows that the landslide body is mainly dry and only a saturated zone occurs at the base of the landslide during high water periods, which minimises the influence of the perched aquifer groundwater level on the destabilisation. Unlike the observed exponential trend of the amplitude and of the mean for the four displacement measurement stations, the meteorological data series does not show any trend over the year. The trend on amplitude (Fig. 4) may be related to a sensitivity increase of the landslide to rainfall triggering impulses (Fig. 6), whereas the trend in mean is not directly dependent on rainfall, accounting for the disturbed state of the landslide. The trend is interpreted as a long-term modification of the landslide mechanical properties. Rock weakening is likely a cause of the long-term creep deformation.

In order to verify the main hypotheses about the hydrological processes highlighted above, a new modelling approach adapted to the overall framework summarised below is needed. The groundwater model should take into account a two-layer aquifer with a reactive perched aquifer overlying an inertial deep aquifer. This pattern is coherent with the conceptual groundwater model of Guglielmi et al. (2002) and Vallet et al. (2015b). In addition, the detrended displacements of the four stations show synchronous seasonal variations with regular amplitude, meaning that the groundwater process responsible of the destabilisation can be considered to be

homogeneous at the Séchilienne landslide scale, leading to use the model as lumped for groundwater processes. The displacement trends indicate that the Séchilienne landslide is subject to a non-linear deformation, showing a standard creep deformation curve that cannot be directly related to the precipitation/recharge input. The four displacement measurement stations show significantly different growing patterns on their trends. This spatial variability has to be taken into account in the model. To predict the Séchilienne displacement with only the precipitation time-series, the model must simulate the two identified components: seasonal variations and long-term creep trend. The GLIDE model fulfils these conditions and is applied for Séchilienne.

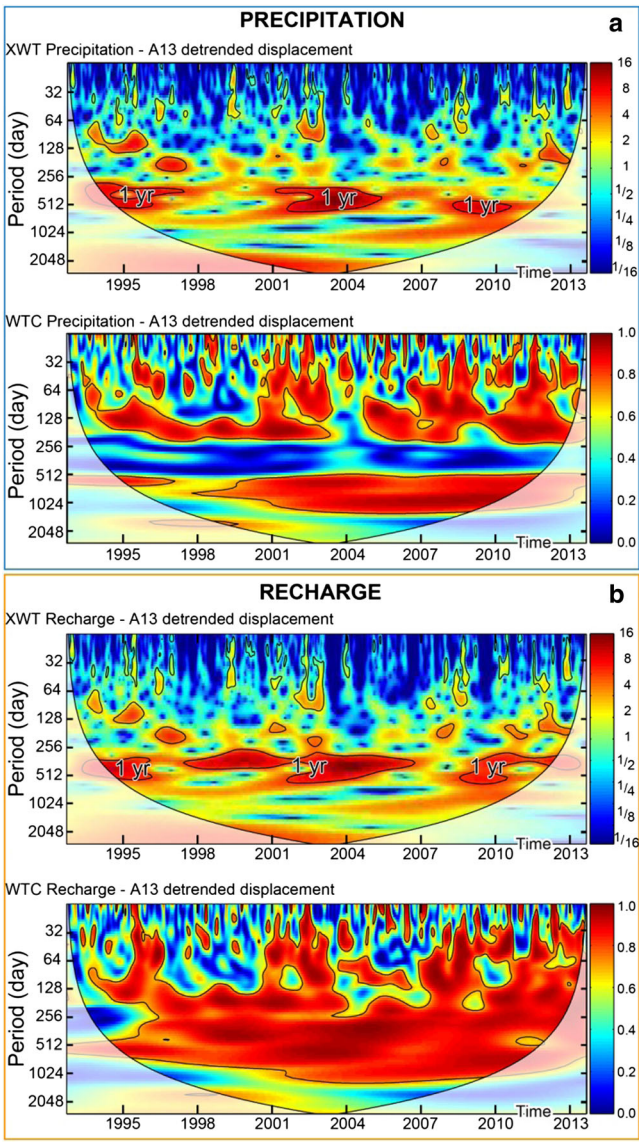

Fig. 6 Cross wavelet (XWT) and wavelet coherence (WTC) spectra with **a** precipitation and A13 detrended displacement and **b** recharge and A13 detrended displacement. The *thick black line* designates the 5 % significance level against red noise. The cone of influence, whose edge effects might distort the picture, is shown by using attenuated colour intensities

Results and implication of the GLIDE model

Model performance

Figure 7 shows the evolution of the performance criteria according to the computation step from 8 to 32 days. Figure 8 illustrates the ability of the model to reproduce observed data for a computation step of 8 days. The model parameter values estimated for scenarios 1 (S1) and 2 (S2) are detailed in Table 1.

Regarding the detrended displacement, S1 shows a better performance than S2 in taking into account the performances on both calibration and validation periods (Fig. 7). For the three performance criteria, a time step above 20 days (average break point) does not improve significantly the model performances. Above this break point, NS_m and NSL_m are always larger than 0.65 and 0.67, respectively, and $RMSE_m$ are lower than 0.23 (Fig. 7). The model shows similar performance for the displacement trend and for raw displacement. For the two scenarios, the performances are always significantly better on the interval I1 than on the interval I2 (Fig. 7), with the $RMSE_m$ indicator always lower than 1.5 mm/day for the displacement trend and raw displacement (Fig. 7). The performance of S2 is distinguishable from S1 for the I2 interval with a $RMSE_m$ lower than 1 mm/day, meaning that the RMSE criterion is sensitive to the calibration interval. The I2 interval covers periods for which the detrended displacement shows higher values (peaks) than the interval covered by the I1 interval. In contrast to the detrended displacement, the computation time step does not significantly influence the performance of the model for the trend and raw displacement, and no average break points are observed.

The following discussion is based on the results from the modelling for S2 which shows the best performance to model the raw displacements. According to Fig. 8, the modelled detrended displacements reproduce satisfactorily the dynamics of the displacement time-series variations. In particular, peaks and troughs are synchronously simulated, as well as their increasing and decreasing slopes. However, the model fails to reproduce several extreme values (as indicated by the better performance of the NSL_m indicator than that of the NS_m indicator, Fig. 7). The modelled raw displacement fits well the creep trend over most of the studied interval except the last part where the model underestimates the exponential increase (Fig. 8). The calibration process by the mean of the $RMSE_m$ values is significantly dependent on the creep trend (see "Calibration periods and optimization" section), meaning that the model in order to be accurate should be calibrated over the last part of the trend.

The difficulty of the model to faithfully reproduce the exponential trend part in the recent years can be the consequence of two phenomena: (1) the control mechanism of the landslide destabilisation becomes mainly driven by the landslide weight to the detriment of the groundwater pressure or (2) the stress-strain relationship is deeply modified by the rearrangement of the landslide constitutive material. During the summer 2013, the Séchilienne landslide showed a sharp decrease of the displacement velocity (Fig. 8), meaning that the rainfall trigger is still required to accelerate the landslide. Nevertheless, for these two dry periods, the landslide velocities did not return to a normal level (i.e. before the exponential growing). These observations support the second assumption involving indirect hydro-mechanical couplings, i.e. a mutual influence between mechanical and hydraulic processes through changes in landslide constitutive material properties (Rutqvist and Stephansson 2003).

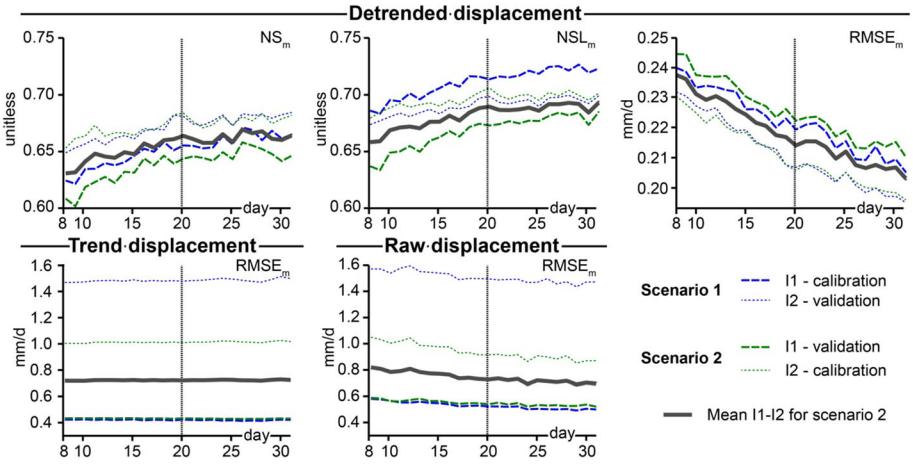

Fig. 7 Evolution of model performances according to a computation time from 8 to 30 days for the two scenarios S1 and S2

Relationship between groundwater pressure and creep deformation

Applied to the Séchilienne landslide, the GLIDE model is able to simulate displacement short-term periodic variations as well as the displacement long-term creep trend. Thus, most of the hydro-mechanical functioning hypotheses are validated. The model shows that the long-term creep deformation mechanism is mainly the consequence of groundwater pressure recurrent variations. Moreover, despite the exponential increase, the Séchilienne landslide destabilisation is not independent from the precipitation trigger. The creep trend is a consequence of indirect hydro-mechanical couplings which modifies the stress-strain relationships.

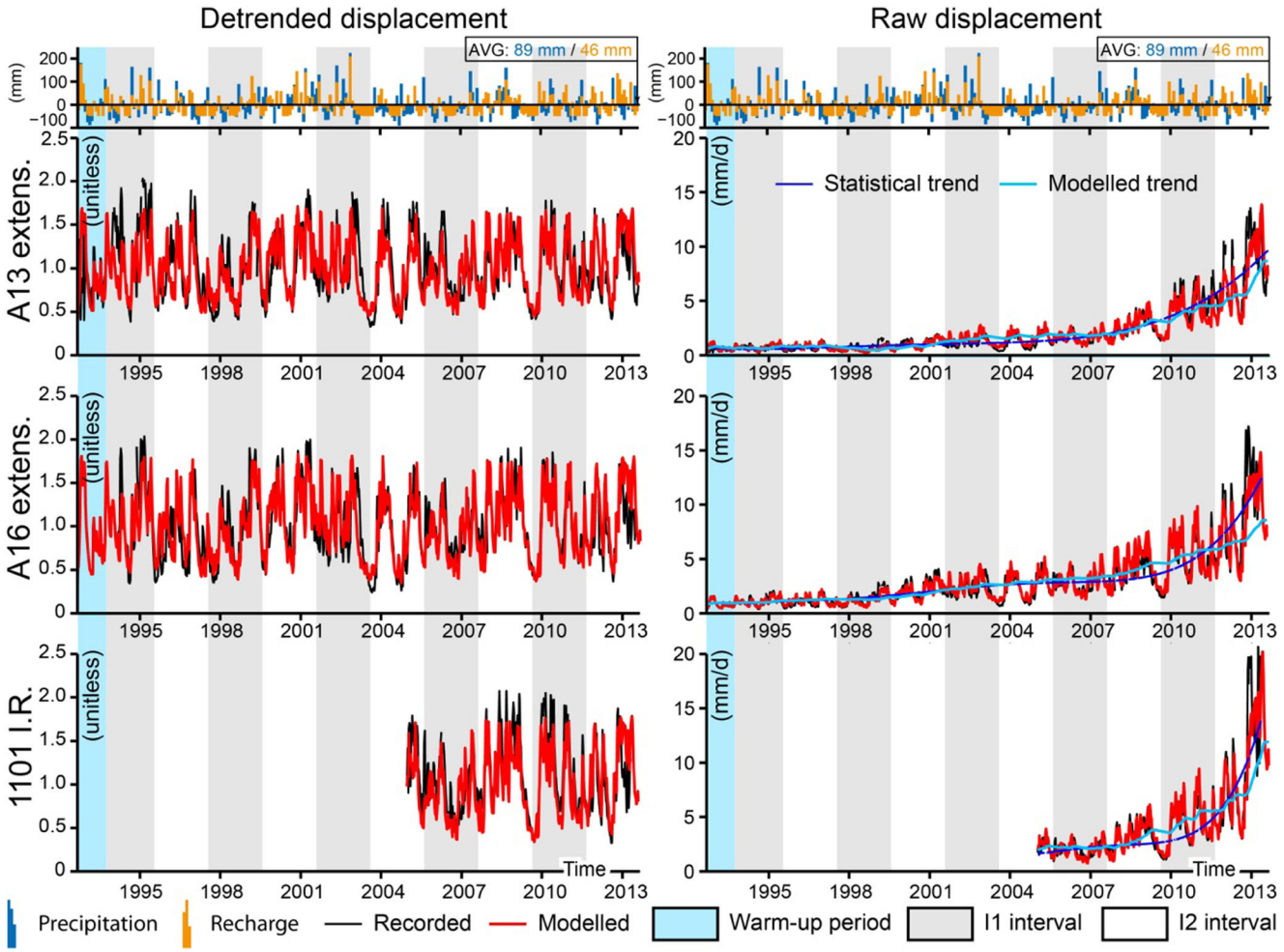

Fig. 8 Simulations of the three displacement recording stations and of the three displacement components (trend, detrended and raw signals) for an 8-day computation time

Model parameter values can give insights about the hydro-mechanical mechanisms they account for and can improve the conceptual groundwater model. The HT corresponds to the 46 % percentile of the WL_c, meaning that the weakening of the Séchilienne landslide occurs over 46 % of the studied interval time. The reservoir recession coefficients, representative of the aquifer permeability, show that the disturbed zone in the perched aquifer has a higher transmissive behaviour (k_p=0.1) than the undamaged bedrock in the deep aquifer (k_d=0.03). This contrast agrees with the occurrence of a reactive perched aquifer in the disturbed zone (Guglielmi et al. 2002). The α triggering coefficient, used to compute the WL_c from the perched (WL_p) and the deep (WL_d) water levels, shows that the Séchilienne destabilisation is triggered at 77 % by the deep aquifer and 23 % by the perched aquifer, while the contribution areas are 98 and 2 %, respectively. This result confirms the dual influence of the two-layer hydrosystem on the destabilisation. This result also shows that the perched aquifer, despite its small surface area, plays a significant role in the destabilisation. However, the main destabilisation triggering role still lies in the deep aquifer, in agreement with Cappa et al. (2014).

The *a* parameter estimates the periodic groundwater triggering impact on the destabilisation for the three stations (A13, 0.37; A16, 0.44; and I1101, 0.44). The rock weakening coefficient β allows to estimate relatively the weakening amount for each station (A13, 1.20×10^{-3}; A16, 7.01×10^{-4}; and I1101, 1.51×10^{-3}). The rock strengthening coefficient γ estimates the consolidation rate for each modelled station (A13, 9.72×10^{-4} mm/day; A16, 2.44×10^{-4} mm/day; and I1101, 1.28×10^{-3} mm/day). Low γ values ($<10^{-3}$ mm/day) mean that periods at rest are better characterised by the absence of weakening processes rather than by physical consolidation. The A13 extensometer is the least influenced by the groundwater pressure, whereas the 1101 infra-red station is the most influenced by the changes of the mechanical properties of the constitutive material showing the higher weakening and strengthening coefficients. This difference cannot be attributed to differing measurement methods (see "Data processing" section). The extensometer A16 shows the lowest strengthening coefficient γ, but this station is reactive to the periodic groundwater stress since it shows the highest α coefficient. The differences between the three stations confirm that local mechanical properties affect significantly the surface deformation and the creep process.

Domain and limits of application of the model

The main asset of the GLIDE model is that it is an easy-to-use approach using a relatively simple parameterization with 16 parameters, of which only 8 parameters have to be calibrated. In contrast with most empirical models (see "Introduction"), GLIDE allows a better understanding of the precipitation-displacement relationship by enabling the simulation of the two displacement components (seasonal variations and creep trend), although it is not able to simulate all the physics of the studied system. Moreover, the good performance of the model allows to overcome problems of missing data for periods up to several years.

Although GLIDE performances for the most recent intervals are not as good as those for the former intervals, it does not mean that the model is not reliable for displacement prediction. Indeed, this study models the precipitation/displacement relationships with the aim of improving the understanding of creep deep-seated landslide functioning. For this purpose, the calibration of the model is performed independently of the trend (see "The case of modelling multiple displacement records" section). For prediction purposes, it would be necessary to calibrate the model with the raw displacement data, i.e. by taking into account the trend influence. This should considerably reduce the error on the prediction of future values.

The main limit of the model lies in the fact that it has been tested only on the Séchilienne landslide, owing to the use of empirical relationships which are based on physical and geometrical characteristics specific to the study site. This may prevent a straightforward application of the model to other sites where the landslide geological or hydrogeological structures are different from that of Séchilienne or where only scarce data are available. Considering that GLIDE is able to predict displacement with a good performance, its ability to be used in an operational early-warning system should be assessed by performing a forecasting procedure such as the one proposed by Bernardie et al. (2014).

Conclusion

The aims of this paper are (i) to characterise hydro-mechanical processes by investigating precipitation-displacement relationships using a wavelet analysis and (ii) to develop a lumped model (GLIDE) to simulate displacement for landslides subject to creep deformation. First, the wavelet analysis applied on raw and detrended dataset allows to define a first conceptual model that shows that the infra-annual detrended displacement results from short duration high intensity precipitation events. Conversely, annual and multi-annual variations, where most of the displacement variability is observed, are rather linked to recharge and thus to groundwater processes. Our approach demonstrates the relevancy of wavelet analysis in characterising the non-linear creep processes for landslides on pluri-annual time-series. Second, the GLIDE model, coupling a groundwater model to a creep landslide model built on this preliminary model, shows good performances to simulate the decomposed displacement time-series into trend and detrended displacement, validating the functioning hypothesis.

The main insights of this study are that (i) the Séchilienne landslide displacement periodic variations are triggered by a dual groundwater layer, with a perched reactive aquifer (responsible of high-frequency displacements) and a deep inertial aquifer (responsible of low frequencies of displacement), and that (ii) although the displacement trend cannot be directly related to the precipitation input, the trend is the consequence of rock mechanical weakening due to recurrent groundwater pressure variations. These results show that the long-term creep deformation is mainly the consequence of the recharge input. Lastly, the good performance of the GLIDE model opens the possibility of further developing early-warning systems for deep-seated landslides.

Acknowledgments

This research was fund by the programme SLAMS (Séchilienne Land movement: Multidisciplinary Studies) of the Agence Nationale de la Recherche. The meteorological and displacement data were supplied by CEREMA Lyon. The authors acknowledge the support of Jean-Pierre Duranthon and Marie-Aurélie Chanut from the CEREMA Lyon. We thank the editor for efficient handling of the manuscript. The manuscript was improved by detailed and constructive comments from three anonymous reviewers.

Appendix—wavelet analysis

Continuous wavelet transforms

The continuous wavelet transform (CWT) $W_x(\tau, a)$ of a time-series $x(t)$ is given as follows:

$$W_x(\tau,\ a) = \int_{-\infty}^{+\infty} x(t)\, \Psi^*_{\tau,\ a}(t)\mathrm{d}t \tag{13}$$

where

$$\Psi_{\tau,\ a} = \frac{1}{\sqrt{a}}\, \Psi\left(\frac{t-\tau}{a}\right) \tag{14}$$

represents a group of wavelet functions, $\Psi_{\tau,\ a}$, based on a mother wavelet Ψ which can be scaled and translated, modifying the scale parameter a and the translation parameter τ, respectively. (*) corresponds to the complex conjugate. Wavelet functions have multi-scale properties, dilating or contracting a (a>1; a<1). When a increases, the wavelet covers a higher signal window. It allows the large-scale behaviour of x to be extracted. Conversely, when a decreases, the analysed signal window decreases, allowing local variations of x to be studied. Wavelet transform is thus characterised on the space scale by a window decreasing in width when we focus on local-scale structures (high frequency) and widening when we focus on large-scale structures (low frequency).

As in the Fourier analysis, a wavelet power spectrum (WPS, also called a scalogram) $P_x(\tau, a)$ can be defined as the wavelet transform of $W_x(\tau, a)$:

$$P_x(\tau,\ a) = \left(W_x(\tau,\ a)\ W^*_x(\tau,\ a)\right) = |W_x(\tau,\ a)|^2 \tag{15}$$

The choice of the appropriate analysis wavelet depends on the nature of the signal and on the type of information to be extracted from the time-series (De Moortel et al. 2004). Statistical significance level was estimated against a red noise model (Torrence and Compo 1998; Grinsted et al. 2004). As CWTs are applied to time-series of finite length, edge effects may appear on the scalogram, leading to the definition of a cone of influence (COI) as the region where such effects are relevant (Torrence and Compo 1998). The COI is marked as a shadow in the scalogram.

The covariance of two time-series x and y is estimated using a cross wavelet spectrum (XWT, also called a cross-scalogram) $W_{xy}(\tau, a)$, which is defined as:

$$W_{xy}(\tau,\ a) = \left(W_x(\tau,\ a)\ W^*_y(\tau,\ a)\right) \tag{16}$$

XWT reveals an area with a high common power value, but Maraun and Kurths (2004) reported that it appears unsuitable for significance testing of the interrelation between two series. These authors recommend the use of wavelet coherence (WTC) which is a measure of the intensity of covariance of the two series in the time-scale space. Beginning with the approach of Torrence and Webster (1999), the WTC of two time-series x and y is defined as:

$$C^2_{xy}(\tau,\ a) = \frac{\left|S\left(a^{-1}W_{xy}(\tau,\ a)\right)\right|^2}{S\left(a^{-1}\left|W_x(\tau,\ a)\right|^2\right)\cdot S\left(a^{-1}\left|W_y(\tau,\ a)\right|^2\right)} \tag{17}$$

where S is a smoothing operator in both time and scale (see Torrence and Webster (1999) and Jevrejeva et al. (2003) for detailed mathematical expressions). The 5 % significance level of WTC against red AR1 noise is estimated using Monte Carlo methods (Grinsted et al. 2004).

Multi-resolution analysis

In order to implement the wavelet transform on sampled signals, the discrete wavelet transform (DWT) can be used to discretise the scale and location parameters j and k, respectively. The discrete form of the wavelet transform of a time-series $x(t)$ is given according to Eq. (18):

$$W_x(\tau_o,\ a_o) = \sum_{-\infty}^{+\infty} x(t)\, \Psi^*_{\tau_o,\ a_o}(t)\mathrm{d}t \tag{18}$$

where

$$\Psi_{\tau_o,\ a_o} = \frac{1}{\sqrt{a_o^j}}\, \Psi\left(\frac{t-ka_o^j\tau_o}{a_o^j}\right) \tag{19}$$

with $a_o{}^j$ being the scale parameter, τ_o the translation parameter and k and j integers. $\Psi^*_{\tau_o,\ a_o}$ corresponds to the complex conjugate of $\Psi_{\tau_o,\ a_o}$.

Multi-resolution analysis (MRA) is able to study signals represented at different resolutions. It can be used to decompose a signal into a progression of successive approximations and details in increasing order of resolution. Choosing particular values of a_o and τ_o, in Eq. (8), namely a_o=2 and τ_o=1, corresponds to the dyadic case used in MRA. The aim is to reduce/increase the resolution by a factor of 2 between two scales. Therefore, the approximation of a signal $x(t)$ at a resolution j, denoted by A_x^j and the detail of the same function at a resolution j, denoted by D_x^j, are defined by:

$$A^j_x(t) = \sum_{k=-\infty}^{+\infty} C_{j,k}\Psi_{j,k}(t) \tag{20}$$

$$D^j_x(t) = \sum_{k=-\infty}^{+\infty} D_{j,k}\Phi_{j,k}(t) \tag{21}$$

where $\Phi_{j,k}(t)$ is a scaled and translated basis function called the scaling function, which is determined with $\Psi_{j,k}(t)$ when a wavelet is selected. $C_{j,k}$ is the scaling coefficient given the discrete sampled values of $x(t)$ at resolution j and location k. It is calculated from $\Phi_{j,k}(t)$ in a similar way for the wavelet coefficient $D_{j,k}$ from $\Psi_{j,k}(t)$ (see Kumar and Foufoula-Georgiou (1997) for detailed mathematical expressions).

The signal $x(t)$ can be reconstructed from the approximation and detail components as:

$$x(t) = A^j_x(t) + \sum_{j=1}^{J} D^j_x(t) \tag{22}$$

where J is the highest resolution level considered. Since MRA ensures that variance is well captured in a limited number of resolution levels, analysis of energy distribution in the sampling time-series across scales gives a good idea of the energy distribution across frequencies.

References

Abellán A, Michoud C, Jaboyedoff M, et al. (2014) Predicting rates of displacement in continuously-moving mass movements. Proceedings of international association engineering geology conference. Springer, Torino (Italy)

Alfonsi P (1997) Relation entre les paramètres hydrologiques et la vitesse dans les glissements de terrains. Exemples de La Clapière et de Séchilienne Revue Française de Géotechnique 79:3–12

Allen RE, Pereira LS, Raes D, Smith M (1998) Crop evapotranspiration: guidelines for computing crop water requirements, FAO irrigation and drainage paper 56. Food and Agriculture Organization of the United Nations, Rome

Angeli MG, Buma J, Gasparetto P, Pasuto A (1998) A combined hillslope hydrology/stability model for low-gradient clay slopes in the Italian dolomites. Eng Geol 49:1–13. doi:10.1016/S0013-7952(97)00033-1

Angeli MG, Gasparetto P, Bromhead E (2004) Strength-regain mechanisms in intermittently moving landslides. Proceedings of the 9th international symposium on landslides. Taylor & Francis, London, Rio de Janeiro, pp 689–696

Aragon Y (2011) Séries temporelles avec R: Méthodes et cas, Édition : Reprint. Springer Editions, Paris

Belle P, Aunay B, Bernardie S et al (2014) The application of an innovative inverse model for understanding and predicting landslide movements (Salazie cirque landslides, Reunion Island). Landslides 11:343–355. doi:10.1007/s10346-013-0393-5

Bernardie S, Desramaut N, Malet J-P, et al. (2014) Prediction of changes in landslide rates induced by rainfall. Landslides 1–14 10.1007/s10346-014-0495-8

Bertsimas D, Tsitsiklis J (1993) Simulated annealing. Statist Sci 8:10–15. doi:10.1214/ss/1177011077

Beven K (2006) A manifesto for the equifinality thesis. J Hydrol 320:18–36. doi:10.1016/j.jhydrol.2005.07.007

Binet S, Guglielmi Y, Bertrand C, Mudry J (2007) Unstable rock slope hydrogeology: insights from the large-scale study of western Argentera-Mercantour hillslopes (South-East France). Bull Soc Geol Fr 178:159–168. doi:10.2113/gssgfbull.178.2.159

Bogaard T, Guglielmi Y, Marc V et al (2007) Hydrogeochemistry in landslide research: a review. Bull Soc Geol Fr 178:113–126. doi:10.2113/gssgfbull.178.2.113

Bonzanigo L, Eberhardt E, Loew S (2007) Long-term investigation of a deep-seated creeping landslide in crystalline rock. Part I. Geological and hydromechanical factors controlling the Campo Vallemaggia landslide. Can Geotech J 44:1157–1180. doi:10.1139/T07-043

Brückl EP (2001) Cause-effect models of large landslides. Nat Hazards 23:291–314. doi:10.1023/A:1011160810423

Brückl E, Brunner FK, Lang E et al (2013) The Gradenbach Observatory—monitoring deep-seated gravitational slope deformation by geodetic, hydrological, and seismological methods. Landslides 10:815–829. doi:10.1007/s10346-013-0417-1

Brunsden D (2001) A critical assessment of the sensitivity concept in geomorphology. CATENA 42:99–123. doi:10.1016/S0341-8162(00)00134-X

Cappa F, Guglielmi Y, Soukatchoff VM et al (2004) Hydromechanical modeling of a large moving rock slope inferred from slope levelling coupled to spring long-term hydrochemical monitoring: example of the La Clapière landslide (Southern Alps, France). J Hydrol 291:67–90. doi:10.1016/j.jhydrol.2003.12.013

Cappa F, Guglielmi Y, Viseur S, Garambois S (2014) Deep fluids can facilitate rupture of slow-moving giant landslides as a result of stress transfer and frictional weakening. Geophys Res Lett 41:61–66. doi:10.1002/2013GL058566

Č erný V (1985) Thermodynamical approach to the traveling salesman problem: an efficient simulation algorithm. J Optim Theory Appl 45:41–51. doi:10.1007/BF00940812

Chanut M-A, Vallet A, Dubois L, Duranthon J-P (2013) Mouvement de versant de Séchilienne: relations entre déplacements de surface et précipitations – analyse statistique. Journées Aléa Gravitaire 2013. Grenoble, France

Charlier J-B, Bertrand C, Binet S et al (2010) Use of continuous measurements of dissolved organic matter fluorescence in groundwater to characterize fast infiltration through an unstable fractured hillslope (Valabres rockfall, French Alps). Hydrogeol J 18:1963–1969. doi:10.1007/s10040-010-0670-5

Charlier J-B, Bertrand C, Mudry J (2012) Conceptual hydrogeological model of flow and transport of dissolved organic carbon in a small Jura karst system. J Hydrol 460–461:52–64. doi:10.1016/j.jhydrol.2012.06.043

Charlier J-B, Ladouche B, Maréchal J-C (2015) Identifying the impact of climate and anthropic pressures on karst aquifers using wavelet analysis. J Hydrol 523:610–623. doi:10.1016/j.jhydrol.2015.02.003

Chigira M (1992) Long-term gravitational deformation of rocks by mass rock creep. Eng Geol 32:157–184. doi:10.1016/0013-7952(92)90043-X

Corominas J, Moya J, Ledesma A et al (2005) Prediction of ground displacements and velocities from groundwater level changes at the Vallcebre landslide (Eastern Pyrenees, Spain). Landslides 2:83–96. doi:10.1007/s10346-005-0049-1

Cowpertwait PSP, Metcalfe A (2009) Introductory time series with R, Édition : 2009. Springer, New York

Crosta GB, Frattini P, Castellanza R, et al. (2015) Investigation, monitoring and modelling of a rapidly evolving rockslide: the Mt. de la Saxe case study. In: Lollino G, Giordan D, Crosta GB, et al. (eds) Engineering geology for society and territory—volume 2. Springer International Publishing, pp 349–354

de Blasio FV (2011) Introduction to the physics of landslides: lecture notes on the dynamics of mass wasting. Springer, New York

De Moortel I, Munday SA, Hood AW (2004) Wavelet analysis: the effect of varying basic wavelet parameters. Sol Phys 222:203–228. doi:10.1023/B:SOLA.0000043578.01201.2d

Du J, Yin K, Lacasse S (2013) Displacement prediction in colluvial landslides, Three Gorges Reservoir, China. Landslides 10:203–218. doi:10.1007/s10346-012-0326-8

Duranthon JP, Effendiaz L, Memier M, Previtali I (2003) Apport des méthodes topographiques et topométriques au suivi du versant rocheux instable des ruines de Séchilienne. Association Francaise de Topographie 31–38

Durville JL, Kasperki J, Duranthon JP (2009) The Séchilienne landslide: monitoring and kinematics. First Italian Workshop on Landslides. Napoli, Italia, pp 174–180

Federico A, Popescu M, Elia G et al (2012) Prediction of time to slope failure: a general framework. Environ Earth Sci 66:245–256. doi:10.1007/s12665-011-1231-5

Fukuzono T (1985) A new method for predicting the failure time of a slope. In: Proceedings of the 4th International Conference and Field Workshop in Landslides, Tokyo. pp 145–150

Grinsted A, Moore JC, Jevrejeva S (2004) Application of the cross wavelet transform and wavelet coherence to geophysical time series. Nonlinear Process Geophys 11:561–566. doi:10.5194/npg-11-561-2004

Guglielmi Y, Vengeon JM, Bertrand C et al (2002) Hydrogeochemistry: an investigation tool to evaluate infiltration into large moving rock masses (case study of La Clapière and Séchilienne alpine landslides). Bull Eng Geol Environ 61:311–324

Guglielmi Y, Cappa F, Binet S (2005) Coupling between hydrogeology and deformation of mountainous rock slopes: insights from La Clapière area (southern Alps, France). Compt Rendus Geosci 337:1154–1163. doi:10.1016/j.crte.2005.04.016

Guillot S, di Paola S, Ménot R-P et al (2009) Suture zones and importance of strike-slip faulting for Variscan geodynamic reconstructions of the external crystalline massifs of the western Alps. Bull Soc Geol Fr 180:483–500. doi:10.2113/gssgfbull.180.6.483

Huang A-B, Lee J-T, Ho Y-T et al (2012) Stability monitoring of rainfall-induced deep landslides through pore pressure profile measurements. Soils Found 52:737–747. doi:10.1016/j.sandf.2012.07.013

Iverson RM (2000) Landslide triggering by rain infiltration. Water Resour Res 36:1897–1910. doi:10.1029/2000WR900090

Jevrejeva S, Moore JC, Grinsted A (2003) Influence of the Arctic Oscillation and El Niño-Southern Oscillation (ENSO) on ice conditions in the Baltic Sea: the wavelet approach. J Geophys Res 108:4677. doi:10.1029/2003JD003417

Kirkpatrick S, Gelatt CD, Vecchi MP (1983) Optimization by simulated annealing. Science 220:671–680. doi:10.1126/science.220.4598.671

Klemeš V (1986) Operational testing of hydrological simulation models. Hydrol Sci J 31:13–24. doi:10.1080/02626668609491024

Klimeš J, Rowberry MD, Blahůt J et al (2011) The monitoring of slow-moving landslides and assessment of stabilisation measures using an optical–mechanical crack gauge. Landslides 9:407–415. doi:10.1007/s10346-011-0306-4

Krause P, Boyle DP, Bäse F (2005) Comparison of different efficiency criteria for hydrological model assessment. Adv Geosci 5:89–97. doi:10.5194/adgeo-5-89-2005

Kumar P, Foufoula-Georgiou E (1997) Wavelet analysis for geophysical applications. Rev Geophys 35:385–412. doi:10.1029/97RG00427

Labat D, Ababou R, Mangin A (2000) Rainfall–runoff relations for karstic springs part II: continuous wavelet and discrete orthogonal multiresolution analyses. J Hydrol 238:149–178. doi:10.1016/S0022-1694(00)00322-X

Le Roux O (2009) Caractérisation de l'évolution géomorphologique de la basse vallée de la Romanche en relation avec les instabilités gravitaires de ses versants rocheux. Université Joseph-Fourier - Grenoble I

Le Roux O, Jongmans D, Kasperski J et al (2011) Deep geophysical investigation of the large Séchilienne landslide (Western Alps, France) and calibration with geological data. Eng Geol 120:18–31. doi:10.1016/j.enggeo.2011.03.004

Lebrouc V, Schwartz S, Baillet L et al (2013) Modeling permafrost extension in a rock slope since the Last Glacial Maximum: application to the large Séchilienne landslide (French Alps). Geomorphology 198:189–200. doi:10.1016/j.geomorph.2013.06.001

Li T, Chen M, Wang L, Zhou Y (1996) Time prediction of landslides using Verhulst inverse-function model. Proceedings of the 7th international symposium on landslides. Trondheim, pp 1289–1293

Liu X, Zeng X-H, Liu C-Y (2005) Research on artificial neural network-time series analysis of slope nonlinear displacement. Yanshilixue Yu Gongcheng Xuebao/Chin J Rock Mech Eng 24:3499–3504

Madsen H (2007) Time series analysis, 1 edition. Chapman and Hall/CRC, Boca Raton

Malet J-P, van Asch TWJ, van Beek R, Maquaire O (2005) Forecasting the behaviour of complex landslides with a spatially distributed hydrological model. Nat Hazards Earth Syst Sci 5:71–85. doi:10.5194/nhess-5-71-2005

Maraun D, Kurths J (2004) Cross wavelet analysis: significance testing and pitfalls. Nonlinear Process Geophys 11:505–514. doi:10.5194/npg-11-505-2004

Massei N, Dupont JP, Mahler BJ et al (2006) Investigating transport properties and turbidity dynamics of a karst aquifer using correlation, spectral, and wavelet analyses. J Hydrol 329:244–257. doi:10.1016/j.jhydrol.2006.02.021

Matsuura S, Asano S, Okamoto T (2008) Relationship between rain and/or meltwater, pore-water pressure and displacement of a reactivated landslide. Eng Geol 101:49–59. doi:10.1016/j.enggeo.2008.03.007

Ménot R-P (1988) The geology of the Belledonne massif: an overview (external crystalline massifs of the western Alps). Swiss J Geosci 68:529–540

Meric O, Garambois S, Jongmans D et al (2005) Application of geophysical methods for the investigation of the large gravitational mass movement of Séchilienne, France. Can Geotech J 42:1105–1115. doi:10.1139/t05-034

Monjuvent G, Winistörfer J (1980) Glaciations quaternaires dans les Alpes franco-suisses et leur piedmont. France

Nash JE, Sutcliffe JV (1970) River flow forecasting through conceptual models part I—a discussion of principles. J Hydrol 10:282–290. doi:10.1016/0022-1694(70)90255-6

Nieuwenhuis JD (1991) Variations in stability and displacements of a shallow seasonal landslide in varved clays. Utrecht University

Petley DN, Petley DJ (2006) On the initiation of large rockslides: perspectives from a new analysis of the Vaiont movement record. In: Evans SG, Mugnozza GS, Strom A, Hermanns RL (eds) Landslides from massive rock slope failure. Springer, Netherlands, pp 77–84

Pisani G, Castelli M, Scavia C (2010) Hydrogeological model and hydraulic behaviour of a large landslide in the Italian Western Alps. Nat Hazards Earth Syst Sci 10:2391–2406. doi:10.5194/nhess-10-2391-2010

Prokešová R, Medved'ová A, Tábořík P, Snopková Z (2013) Towards hydrological triggering mechanisms of large deep-seated landslides. Landslides 10:239–254. doi:10.1007/s10346-012-0330-z

Rochet L, Giraud A, Antoine P, Évrard H (1994) La déformation du versant sud du Mont-Sec dans le secteur des ruines de Séchilienne (Isère). Bull Int Assoc Eng Geol 50:75–87. doi:10.1007/BF02594959

Rutqvist J, Stephansson O (2003) The role of hydromechanical coupling in fractured rock engineering. Hydrogeol J 11:7–40. doi:10.1007/s10040-002-0241-5

Saito M (1969) Research on forecasting the time of occurrence of slope failure. Railway Tech Res Ins Quarterly Rep 10:135–141

Tacher L, Bonnard C, Laloui L, Parriaux A (2005) Modelling the behaviour of a large landslide with respect to hydrogeological and geomechanical parameter heterogeneity. Landslides 2:3–14. doi:10.1007/s10346-004-0038-9

Torrence C, Compo GP (1998) A practical guide to wavelet analysis. Bull Am Meteorol Soc 79:61–78. doi:10.1175/1520-0477(1998)079<0061:APGTWA>2.0.CO;2

Torrence C, Webster PJ (1999) Interdecadal changes in the ENSO–monsoon system. J Clim 12:2679–2690. doi:10.1175/1520-0442(1999)012<2679:ICITEM>2.0.CO;2

Vallet A, Bertrand C, Fabbri O, Mudry J (2015a) An efficient workflow to accurately compute groundwater recharge for the study of rainfall-triggered deep-seated landslides, application to the Séchilienne unstable slope (western Alps). Hydrol Earth Syst Sci 19:427–449. doi:10.5194/hess-19-427-2015

Vallet A., Bertrand C., Mudry J., Bogaard T., Fabbri O., Baudement C., Régent B. (2015b) Contribution of time-related environmental tracing combined with tracer tests for characterization of a groundwater conceptual model: a case study at the Séchilienne landslide, western Alps (France). Hydrogeology journal (in press)

Van Asch TWJ, Buma J, van Beek LP (1999) A view on some hydrological triggering systems in landslides. Geomorphology 30:25–32. doi:10.1016/S0169-555X(99)00042-2

Van Asch TWJ, Van Beek LPH, Bogaard TA (2007) Problems in predicting the mobility of slow-moving landslides. Eng Geol 91:46–55. doi:10.1016/j.enggeo.2006.12.012

Vengeon JM (1998) Déformation et rupture des versants en terrain métamorphique anisotrope: Apport de l'étude des Ruines de Séchilienne. PhD thesis, Université Joseph Fourier I

Zangerl C, Eberhardt E, Perzlmaier S (2010) Kinematic behaviour and velocity characteristics of a complex deep-seated crystalline rockslide system in relation to its interaction with a dam reservoir. Engineering Geology 112:53–67. doi:10.1016/j.enggeo.2010.01.001

A. Vallet (✉) · O. Fabbri · C. Bertrand · N. Carry · J. Mudry
CNRS: UMR6249 Chrono-Environnement,
Université Bourgogne Franche-Comté, 16 route de Gray, 25030, Besançon cedex, France
e-mail: aurelien.vallet@univ-fcomte.fr

J. B. Charlier
BRGM, 1039 Rue de Pinville, 34000, Montpellier, France